ROCHESTER IMAGING CONSORTIUM

ELECTRONIC IMAGING

FINAL BRIEFING REPORT

RESEARCH SUPPORTED IN PART BY THE

U.S. ARMY RESEARCH OFFICE
P-24749-PH
P-24626-PH-UIR

NOVEMBER 1991

NICHOLAS GEORGE
PRINCIPAL INVESTIGATOR
THE INSTITUTE OF OPTICS

COLLEGE OF ENGINEERING AND APPLIED SCIENCE
UNIVERSITY OF ROCHESTER
ROCHESTER, NEW YORK

REPORT DOCUMENTATION PAGE

Form Approved
OMB No. 0704-0188

1. AGENCY USE ONLY (Leave blank)	2. REPORT DATE	3. REPORT TYPE AND DATES COVERED
	Nov. 1991	

4. TITLE AND SUBTITLE

Electronic Imaging

5. FUNDING NUMBERS

6. AUTHOR(S)

Nicholas George

7. PERFORMING ORGANIZATION NAME(S) AND ADDRESS(ES)

Institute of Optics
University of Rochester
Rochester, N.Y. 14627

8. PERFORMING ORGANIZATION REPORT NUMBER

9. SPONSORING/MONITORING AGENCY NAME(S) AND ADDRESS(ES)

U. S. Army Research Office
P. O. Box 12211
Research Triangle Park, NC 27709-2211

10. SPONSORING/MONITORING AGENCY REPORT NUMBER

11. SUPPLEMENTARY NOTES

The view, opinions and/or findings contained in this report are those of the author(s) and should not be construed as an official Department of the Army position, policy, or decision, unless so designated by other documentation.

12a. DISTRIBUTION/AVAILABILITY STATEMENT

Approved for public release; distribution unlimited.

12b. DISTRIBUTION CODE

13. ABSTRACT *(Maximum 200 words)*

The report contains abstracts and captioned visuals of research topics that were reported at the Annual Meeting of the Optical Society of America during 3-8 November 1991 held in San Jose, California.

"Facial Recognition Using Image and Transform Representations," Shen-ge Wang and Nicholas George
"Particulate Sorting Using Matched Filters," Scott D. Coston and Nicholas George
"Recovery of Particulate Size Distributions by Inversion of the Optical Transform Pattern," Scott D. Coston and Nicholas George
"Beam Splitter Cube for White-Light Interferometry," Keith B. Farr and Nicholas George
"Backscatter from a Tilted Rough Disc," Donald J. Schertler and Nicholas George
"Image Deblurring for Multiple-Point Impulse Responses," Bryan J. Stossel and Nicholas George

14. SUBJECT TERMS

Pattern recognition, faces, particulate sizing, remote sensing, backscattering cross-section, image recovery, multiple-point PSF, *ELECTRONIC IMAGING

15. NUMBER OF PAGES

95

16. PRICE CODE

17. SECURITY CLASSIFICATION OF REPORT	18. SECURITY CLASSIFICATION OF THIS PAGE	19. SECURITY CLASSIFICATION OF ABSTRACT	20. LIMITATION OF ABSTRACT
UNCLASSIFIED	UNCLASSIFIED	UNCLASSIFIED	UL

NSN 7540-01-280-5500

92 2 14 113

Standard Form 298 (Rev. 2-89)
Prescribed by ANSI Std. Z39-18
298-102

ROCHESTER IMAGING CONSORTIUM

ELECTRONIC IMAGING

FINAL BRIEFING REPORT

RESEARCH SUPPORTED IN PART BY THE

U.S. ARMY RESEARCH OFFICE
P-24749-PH
P-24626-PH-UIR

NOVEMBER 1991

NICHOLAS GEORGE
PRINCIPAL INVESTIGATOR
THE INSTITUTE OF OPTICS

COLLEGE OF ENGINEERING AND APPLIED SCIENCE
UNIVERSITY OF ROCHESTER
ROCHESTER, NEW YORK

ELECTRONIC IMAGING

FINAL BRIEFING REPORT

The report contains abstracts of research topics that were reported at the Annual Meeting of the Optical Society of America during 3-8 November 1991 held in San Jose, California. Please contact Dr. Nicholas George if you would like further information (716-275-2417). The research described herein was supported in part by the U.S. Army Research Office.

TABLE OF CONTENTS

FACIAL RECOGNITION USING IMAGE AND TRANSFORM REPRESENTATIONS

FACIAL RECOGNITION USING IMAGE AND TRANSFORM REPRESENTATIONS

Shen-ge Wang and Nicholas George

Institute of Optics
University of Rochester
Rochester, NY 14627

ABSTRACT

Automatic recognition of faces is now a reality. In our experiments we seek to establish bounds on the information content required as a function of the configuration of the "machine." In general with the direct image, excellent recognition is obtained for information capacity below Harmon's (1973) benchmark value of 500. Our main data base is gathered from 25 people consisting of three views (front, 30° turn, 60° turn) and 10 separate exposures for each view. Typically, these are grouped into a learning set of 5 and a testing set of 5. In the first series of experiments, an optical Fourier transform configuration is used which includes a ring-wedge photodetector interface together with neural-network software. Good recognition is obtained, and we report on the training using front and side views. In the second series of experiments, frame-grabbed images are used, again with the neural network software. Tests are made of the information capacity required as a function of the image coding. Comparative error rates are presented for recognition in the following cases: with 256 grey levels or using global binarization or using an error-diffusion halftoning algorithm. Particularly good results are obtained from the error-diffusion form of the imagery.

FACIAL RECOGNITION USING IMAGE AND TRANSFORM REPRESENTATIONS

SHEN-GE WANG AND NICHOLAS GEORGE

THE INSTITUTE OF OPTICS
UNIVERSITY OF ROCHESTER

NOV. 1991

FACIAL RECOGNITION USING IMAGE AND TRANSFORM REPRESENTATIONS

- NEURAL NETWORK APPROACH
  INFORMATION CAPACITY
- IMAGE AND TRANSFORMS
  OPTICAL CONFIGURATIONS
- EXPERIMENTS
- CONCLUSION

HOW MANY PICTURE ELEMENTS ARE REQUIRED ?

L.D. HARMON (1970)
BELL TELEPHONE LAB.

10 X 14 CHECKERBOARD
3 BITS (8 LEVELS)

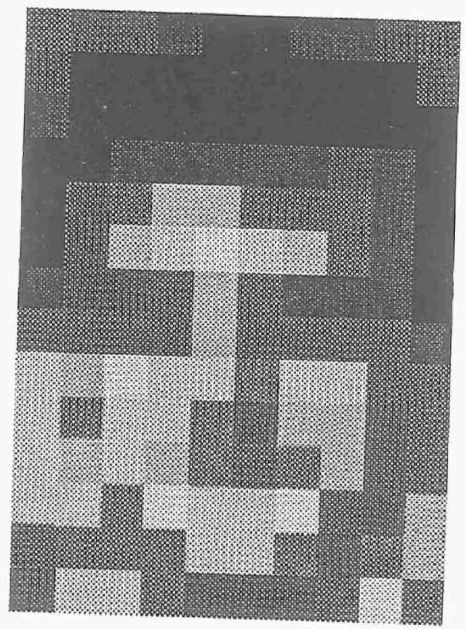

INFORMATION CAPACITY

$C = N \times \text{Log}_2 M$

$= (10 \times 14) \times 3 = 420$

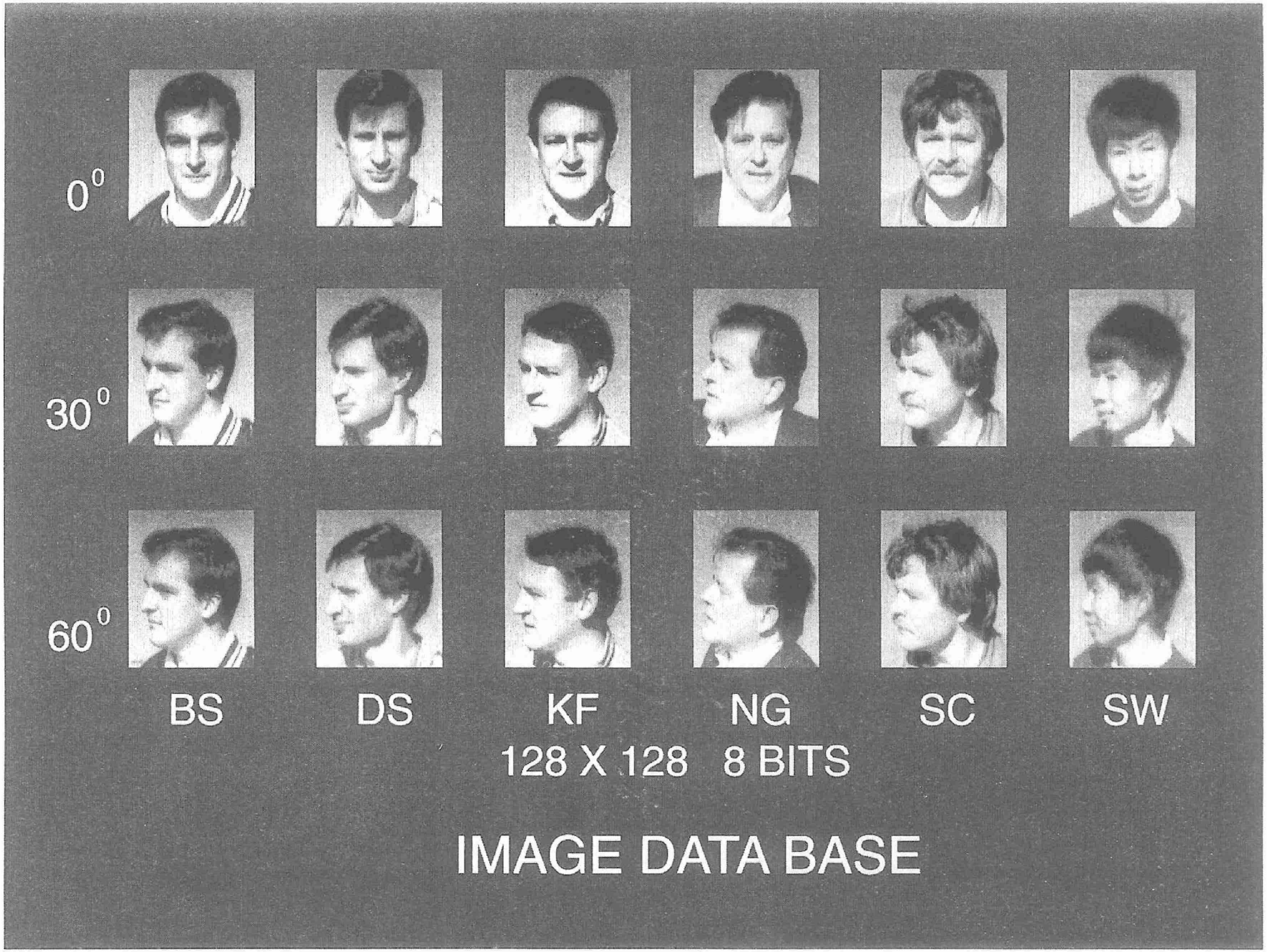
0°
30°
60°
BS
DS
KF
NG
SC
SW
128 X 128 8 BITS
IMAGE DATA BASE

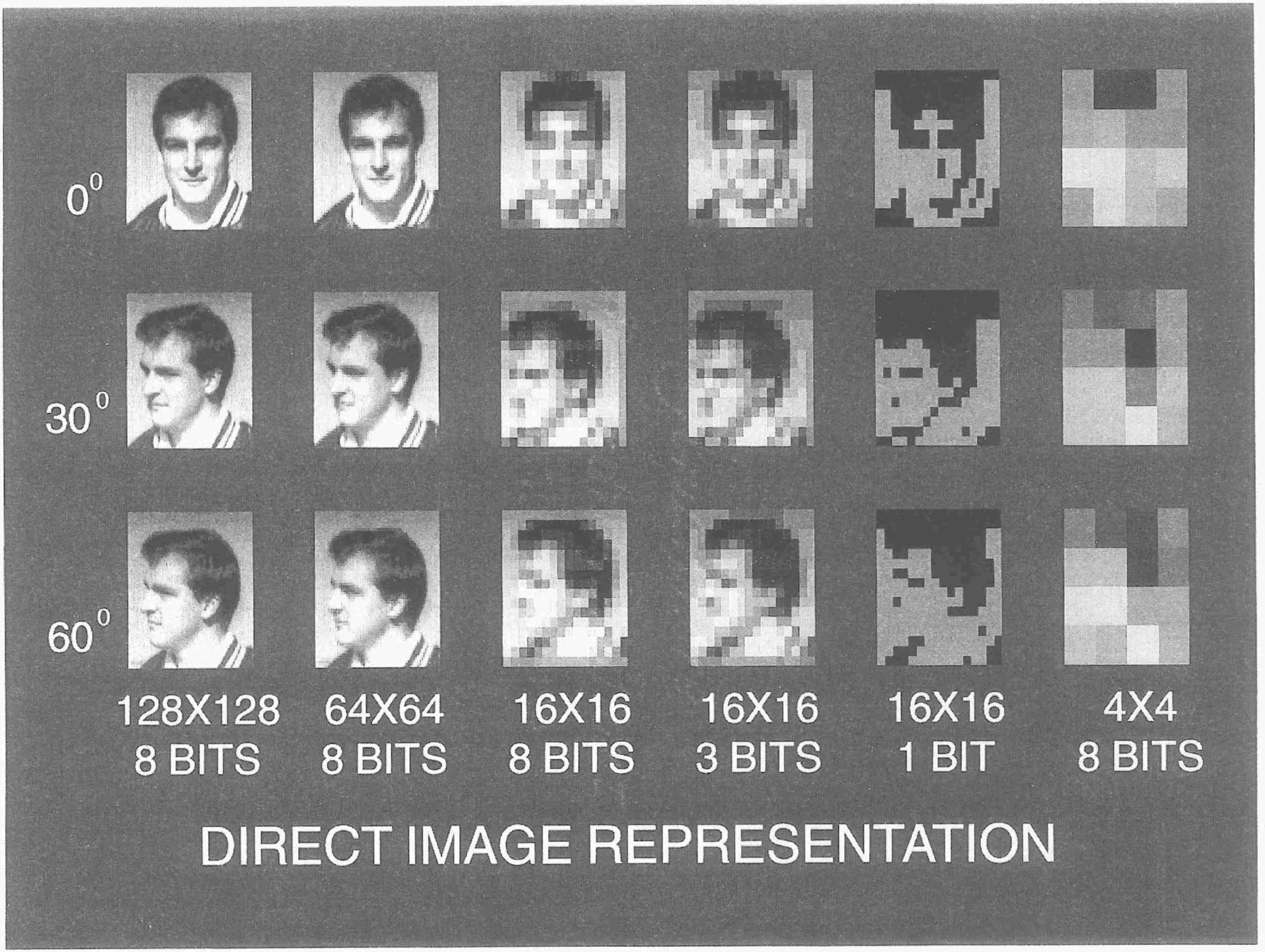
0°
30°
60°
128X128
8 BITS
64X64
8 BITS
16X16
8 BITS
16X16
3 BITS
16X16
1 BIT
4X4
8 BITS
DIRECT IMAGE REPRESENTATION

IMAGE AND OPTICAL FOURIER TRANSFORM (COHERENT ILLUMINATION)

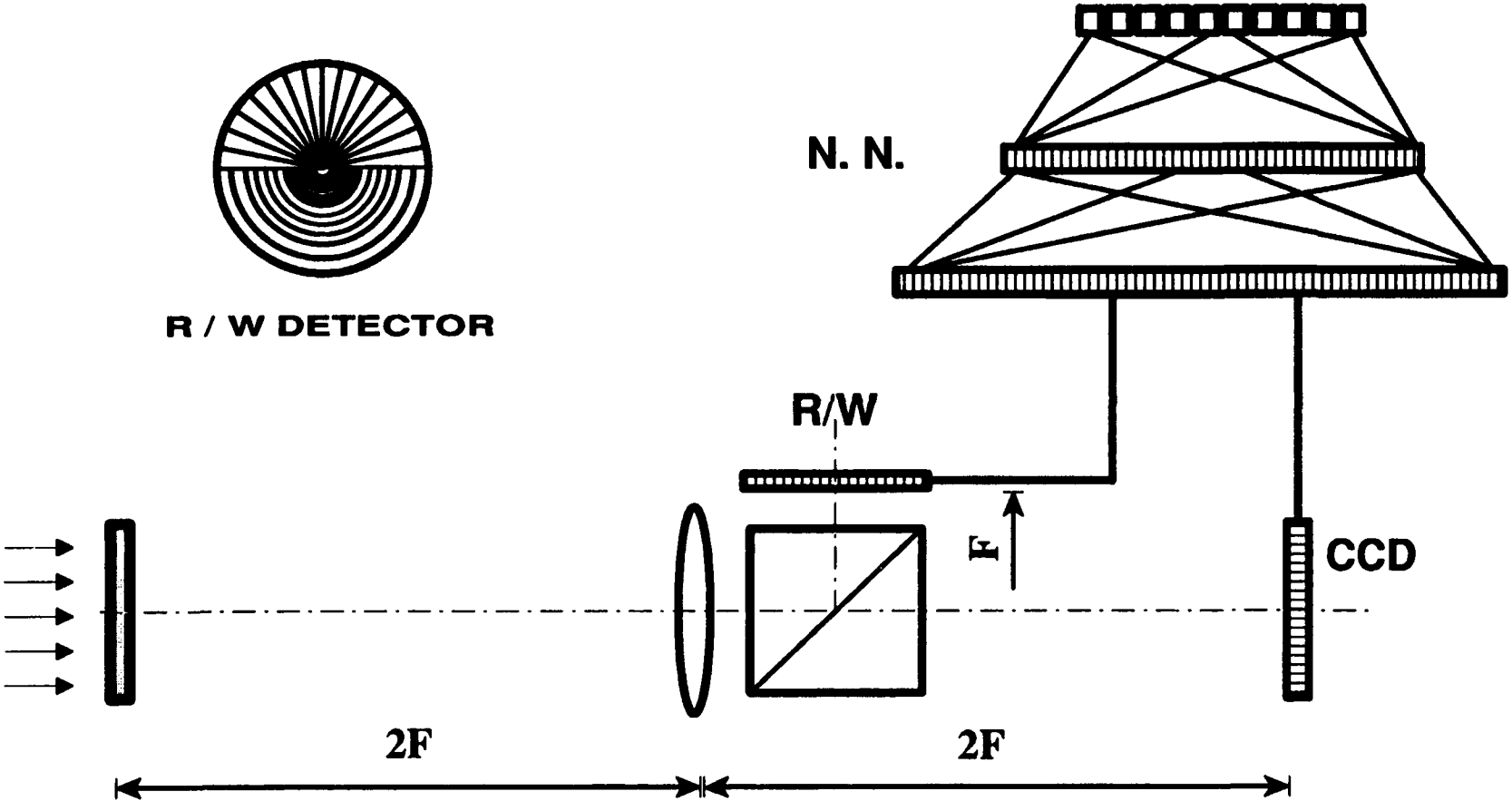

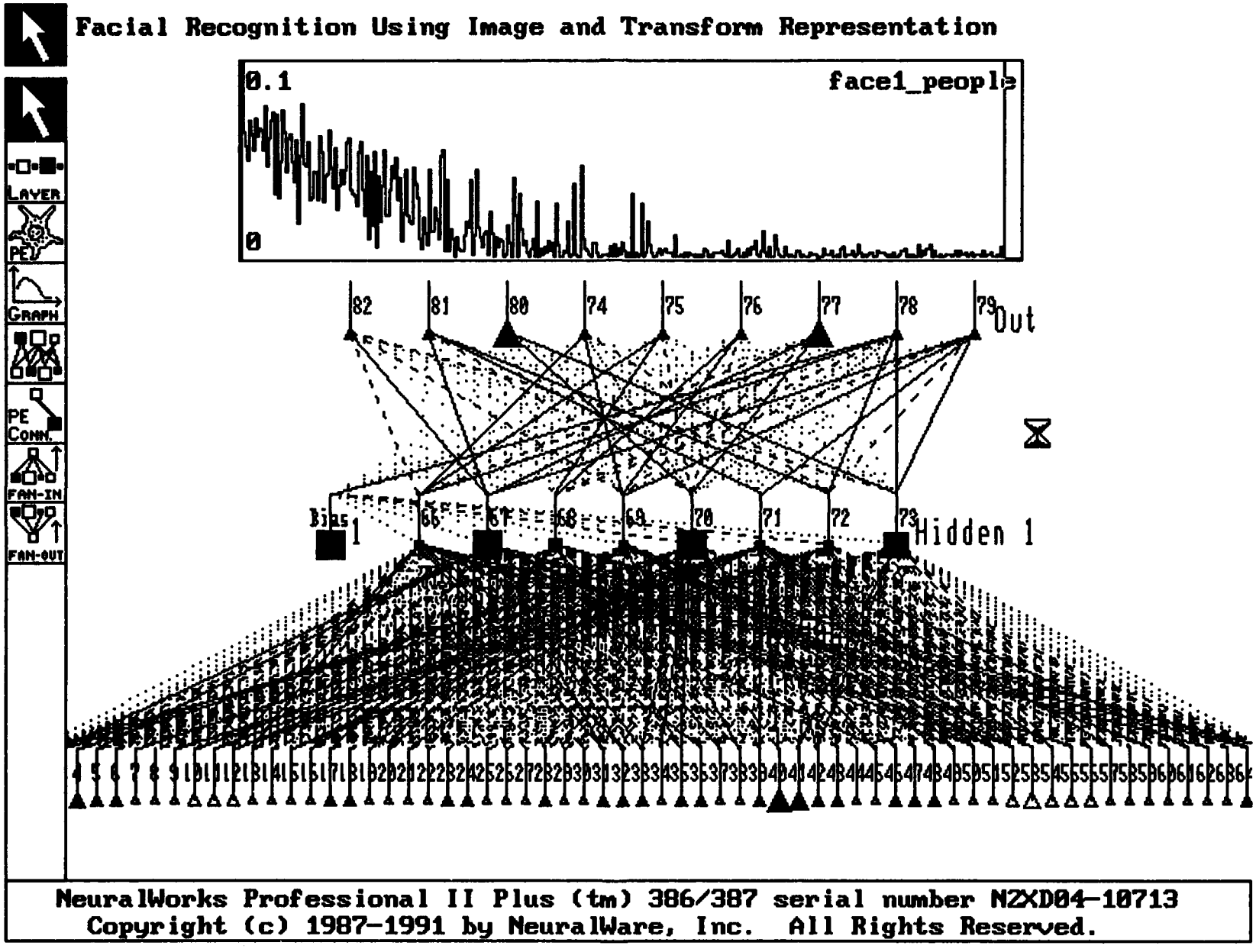
Facial Recognition Using Image and Transform Representation
0.1
face1_people
0
LAYER
PE
GRAPH
PE CONN.
FAN-IN
FAN-OUT
82
81
80
74
75
76
77
78
79
Out
Bias
1
66
67
68
69
70
71
72
73
Hidden 1
NeuralWorks Professional II Plus (tm) 386/387 serial number NZXD04-10713
Copyright (c) 1987-1991 by NeuralWare, Inc. All Rights Reserved.

DIRECT IMAGE: 4X4 ELEMENTS 8 BITS

INPUT		DESIRED OUTPUT																	
		A			B			C			D			E			F		
		0°	30°	60°	0°	30°	60°	0°	30°	60°	0°	30°	60°	0°	30°	60°	0°	30°	60°
A	0°	4																	
	30°		3	***2***															
	60°			4			***1***												
B	0°				4		***1***												
	30°					4	***1***												
	60°						5												
C	0°						***1***	4											
	30°						***1***		4										
	60°			***2***						3									
D	0°										5								
	30°											5							
	60°												5						
E	0°													5					
	30°														4	***1***			
	60°															5			
F	0°																5		
	30°																	4	***1***
	60°																		5

SORTING USING DIRECT IMAGES

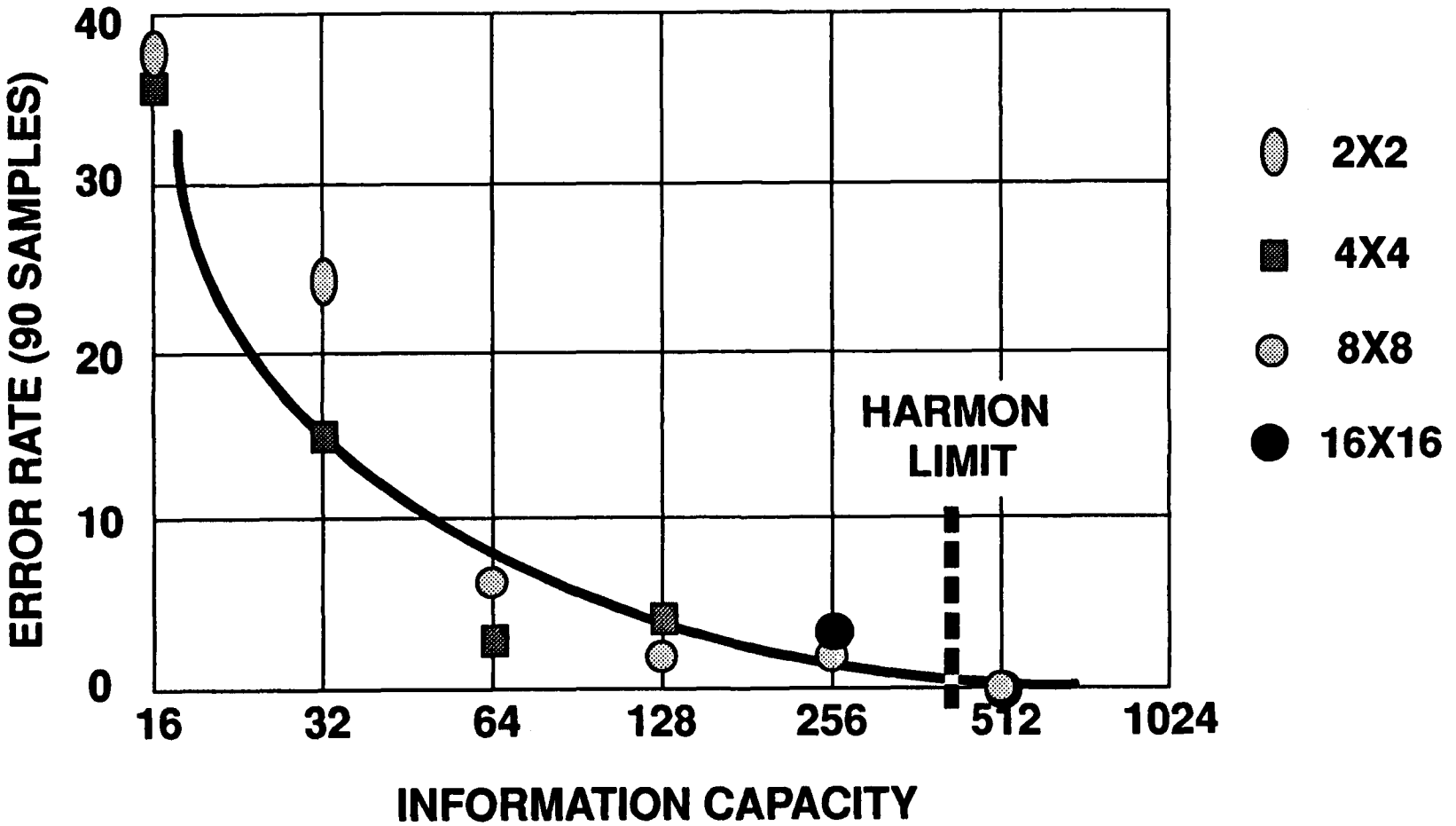

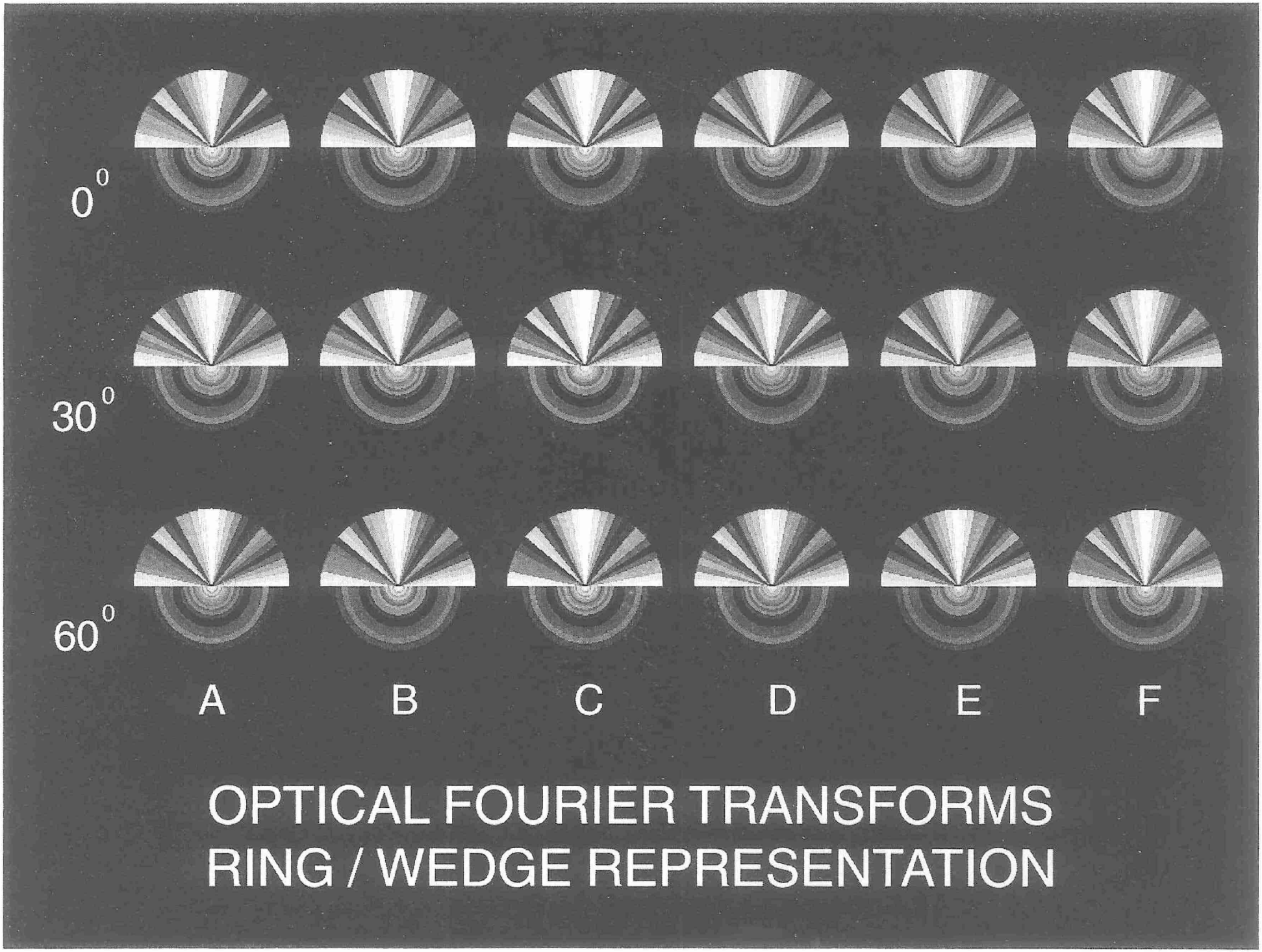
0°
30°
60°
A
B
C
D
E
F
OPTICAL FOURIER TRANSFORMS
RING / WEDGE REPRESENTATION

OPTICAL FOURIER TRANSFORM: 16 R & 16 W

INPUT		DESIRED OUTPUT															
		A			B			C			D			E			F		
		0°	30°	60°	0°	30°	60°	0°	30°	60°	0°	30°	60°	0°	30°	60°	0°	30°	60°
A	0°	5																	
	30°		5																
	60°		*2*	3															
B	0°				5														
	30°					5													
	60°					*3*	2												
C	0°							5											
	30°								5										
	60°									5									
D	0°										5								
	30°											4	*1*						
	60°												5						
E	0°													5					
	30°														3	*2*			
	60°														*3*	2			
F	0°																5		
	30°																	3	*2*
	60°																		5

0^o & 60^o: LEARNING 30^o: TESTING

DIRECT IMAGE: 8X8 ELEMENTS

INPUT		DESIRED OUTPUT					
		A	B	C	D	E	F
A	0^o 30^o 60^o	L 10 L					
B	0^o 30^o 60^o		L 10 L				
C	0^o 30^o 60^o			L 10 L			
D	0^o 30^o 60^o				L 10 L		
E	0^o 30^o 60^o			*1*		L 9 L	
F	0^o 30^o 60^o	*2*					L 8 L

0° & 60°: LEARNING 30°: TESTING

IMAGE: 4X4 + TRANSFORM: 8 R & 8 W

INPUT		DESIRED OUTPUT					
		A	B	C	D	E	F
A	0°	L					
	30°	10					
	60°	L					
B	0°		L				
	30°		10				
	60°		L				
C	0°			L			
	30°			10			
	60°			L			
D	0°				L		
	30°				10		
	60°				L		
E	0°					L	
	30°					10	
	60°					L	
F	0°						L
	30°						10
	60°						L

30°: LEARNING 0° & 60°: TESTING

IMAGE ONLY: 8X8 ELEMENTS

INPUT		DESIRED OUTPUT					
		A	B	C	D	E	F
A	0°	6	*1*	*3*			
	30°	L					
	60°	6	*4*				
B	0°	*2*	4	*4*			
	30°		L				
	60°		10				
C	0°	*1*		9			
	30°			L			
	60°	*2*	*5*	3			
D	0°	*2*		*2*	3	*3*	
	30°				L		
	60°				10		
E	0°			*10*		0	
	30°					L	
	60°				*1*	9	
F	0°	*2*					8
	30°						L
	60°	*1*					9

30°: LEARNING 0° & 60°: TESTING

TRANSFORM ONLY: 32 RINGS & 32 WEDGES

INPUT		DESIRED OUTPUT					
		A	B	C	D	E	F
A	0° 30° 60°	10 L 10					
B	0° 30° 60°		10 L 10				
C	0° 30° 60°	*9*		1 L 10			
D	0° 30° 60°				10 L 10		
E	0° 30° 60°		*1*			0 L 10	*9*
F	0° 30° 60°	*5*	*8* *1*			*3*	2 L 1

30°: LEARNING 0° & 60°: TESTING

IMAGE: 8X8 + TRANSFORM: 32R & 32 W

INPUT		DESIRED OUTPUT					
		A	B	C	D	E	F
A	0° 30° 60°	10 L 10					
B	0° 30° 60°		10 L 10				
C	0° 30° 60°			10 L 10			
D	0° 30° 60°				10 L 10		
E	0° 30° 60°		*5*	*5*		0 L 10	
F	0° 30° 60°						10 L 10

FACIAL RECOGNITION USING IMAGE AND TRANSFORM REPRESENTATIONS

- NEURAL NETWORK PROMISING
- OPTICAL PREPROCESSORS
- SAMPLING AND COMPRESSION

  IN IMAGE & TRANSFORM DOMAINS

PARTICULATE SORTING USING MATCHED FILTERS

PARTICULATE SORTING USING MATCHED FILTERS

Scott D. Coston and Nicholas George

Institute of Optics
University of Rochester
Rochester, NY 14627

ABSTRACT

We present theoretical and experimental results using matched filters to sort between two classes of spherical particles. In particular, matched filters are used to distinguish between dielectric and metal spheres. Three separate light scattering regions are compared in order to identify the best scattering angles. These include the forward, the near forward, and the backscatter regions. Scattering theory is used to calculate the correlation and cross-correlation peaks for the pertinent cases in the output plane of the matched filter. An interesting finding that has not appeared in the literature is that the forward scattering region is an ineffective area in which to use a matched filter for distinguishing between these particles. Of the three scattering regions, the backscatter is shown to be the most effective. Experimental confirmations of these findings have been made using holographic recorded matched filters in a standard Fourier transform configuration. These will be described, including the successful matched filter discrimination utilizing the backscattered radiation.

PARTICULATE SORTING USING MATCHED FILTERS[†]

Scott D. Coston

Nicholas George

The Institute of Optics

University of Rochester

1991

† Presnted at the 1991 Optical Society of America conference in San Jose.

STATEMENT OF THE PROBLEM

- **Use a matched filter to sort spherical particles of different composition.**

- **Determine optimum scattering region for sorting.**

SCATTERING GEOMETRY

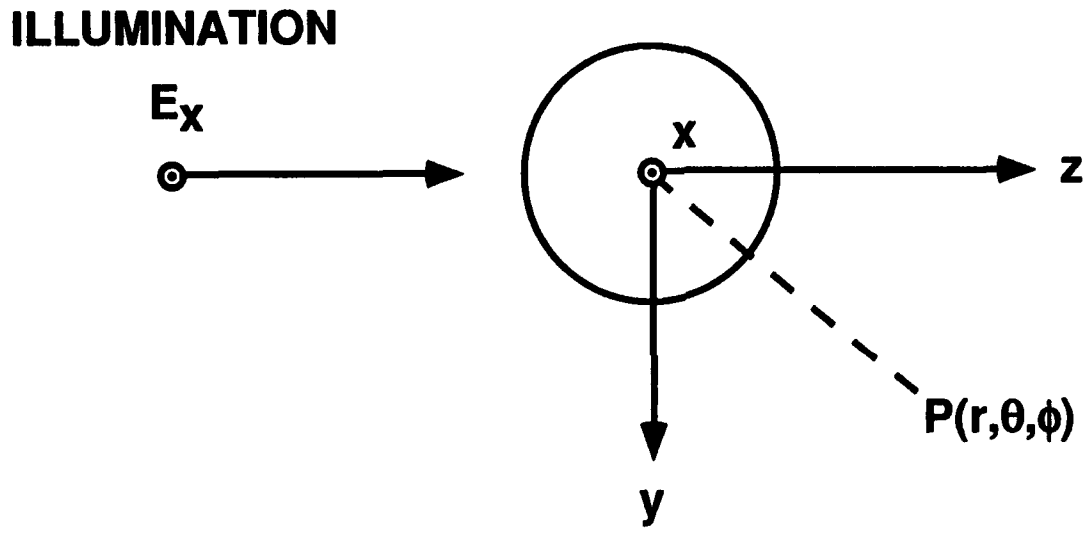

a -- PARTICLE RADIUS
m -- RELATIVE INDEX OF REFRACTION

This figure shows the geometry for scattering of an incident plane wave by a sphere. The sphere is described by the radius **a** and the relative index of refraction of the sphere to the surrounding medium, **m**. The incident plane wave is assumed polarized in the x-direction. The scattered field is calculated at the point P, defined by the spherical coordinates (r,θ,ϕ).

MIE SCATTERING FORMULAS

$$E_\theta = \frac{ie^{-ik_2 r}}{k_2 r}\cos\phi \sum_{n=1}^{\infty}(-1)^{n+1}\frac{2n+1}{n(n+1)}\{a_n\tau_n + b_n\tau\tau_n\}$$

$$E_\phi = -\frac{ie^{-ik_2 r}}{k_2 r}\sin\phi \sum_{n=1}^{\infty}(-1)^{n+1}\frac{2n+1}{n(n+1)}\{a_n\tau\tau_n + b_n\tau_n\}$$

$$a_n = \frac{\psi_n(\alpha)\psi'_n(\beta) - m\psi'_n(\alpha)\psi_n(\beta)}{\psi_n(\alpha)\zeta'_n(\beta) - m\psi'_n(\alpha)\zeta_n(\beta)} \quad \text{and} \quad b_n = \frac{m\psi_n(\alpha)\psi'_n(\beta) - \psi'_n(\alpha)\psi_n(\beta)}{m\psi_n(\alpha)\zeta'_n(\beta) - \psi'_n(\alpha)\zeta_n(\beta)}$$

$$\alpha = k_2 a \quad \text{and} \quad \beta = mk_2 a$$

$$\tau_n = \frac{d}{d\theta}P_n^{(1)}(\cos\theta) \quad \text{and} \quad \tau\tau_n = \frac{P_n^{(1)}(\cos\theta)}{\sin\theta}$$

The scattered fields in the far zone can be calculated using the Mie formulas[1]. The coefficients a_n and b_n contain only information about the sphere, while the functions τ_n and $\tau\tau_n$ contain the angular information. Calculation of the coefficients are accomplished using recursion formulas[2] for a_n, b_n, τ_n, and $\tau\tau_n$.

1.) G. Mie, "Beitrage zur Optik Trüber Medien, Speziell Koloidaler Metallösungen," Ann. Physik 25, 377-445, (1908).
2.) W. D. Ross, "Computation of Bessel Functions in Light Scattering Studies," Appl. Opt. 11, 1919 (1972).

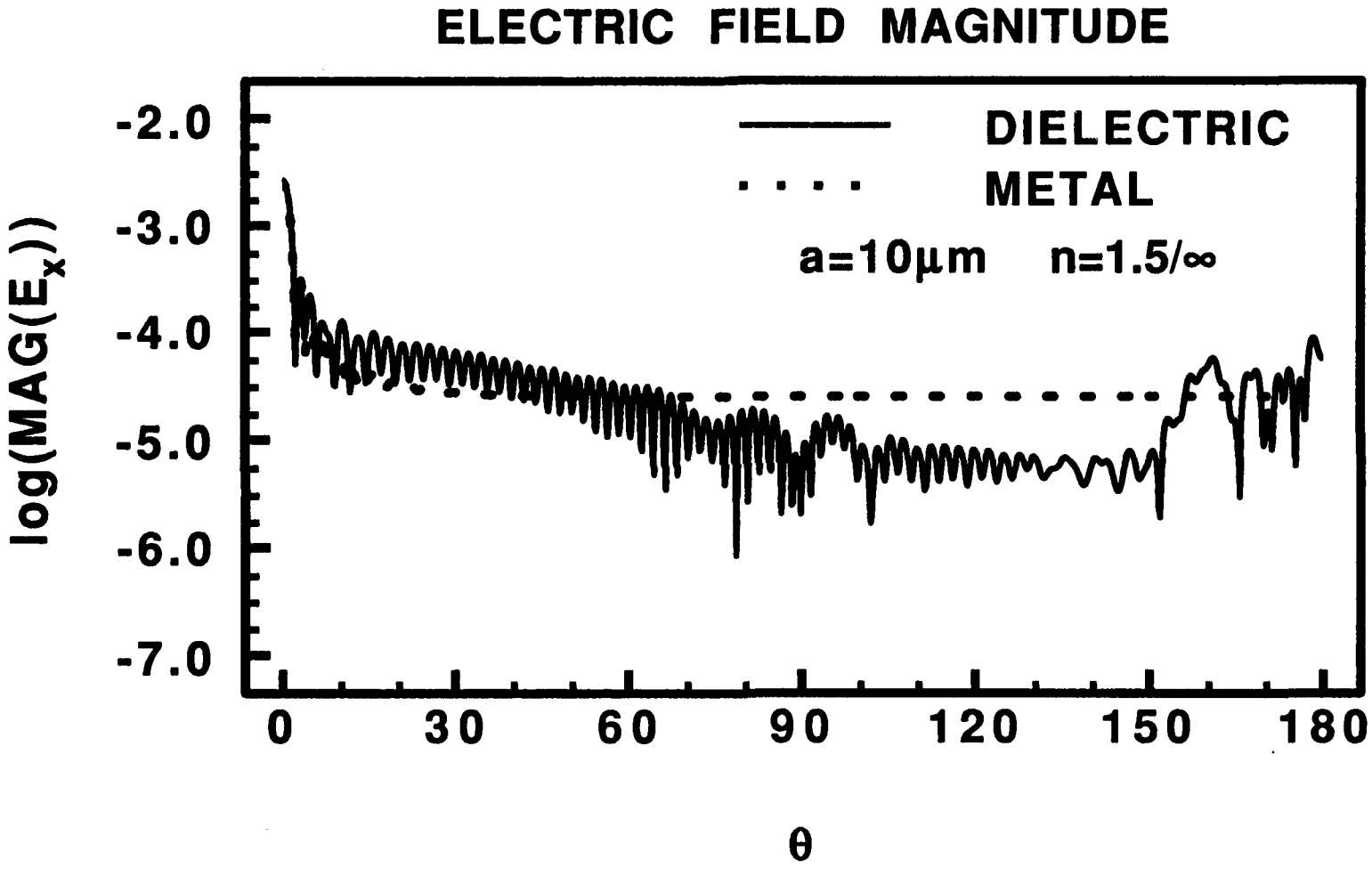

This figure shows the log of the magnitude of the x-polarized scattered field. The solid curves was calculated for a dielectric sphere with index of refraction 1.5. The dashed curve is for a perfectly conducting sphere. Both spheres have a radius of 10 μm. Note the similarity of the two plots near the forward scattering region. Past θ=5°, however, the scattering pattern for the metal sphere decays to a constant value, proportional to the radius, while the scattering pattern for the dielectric sphere continues to oscillate throughout the region shown.

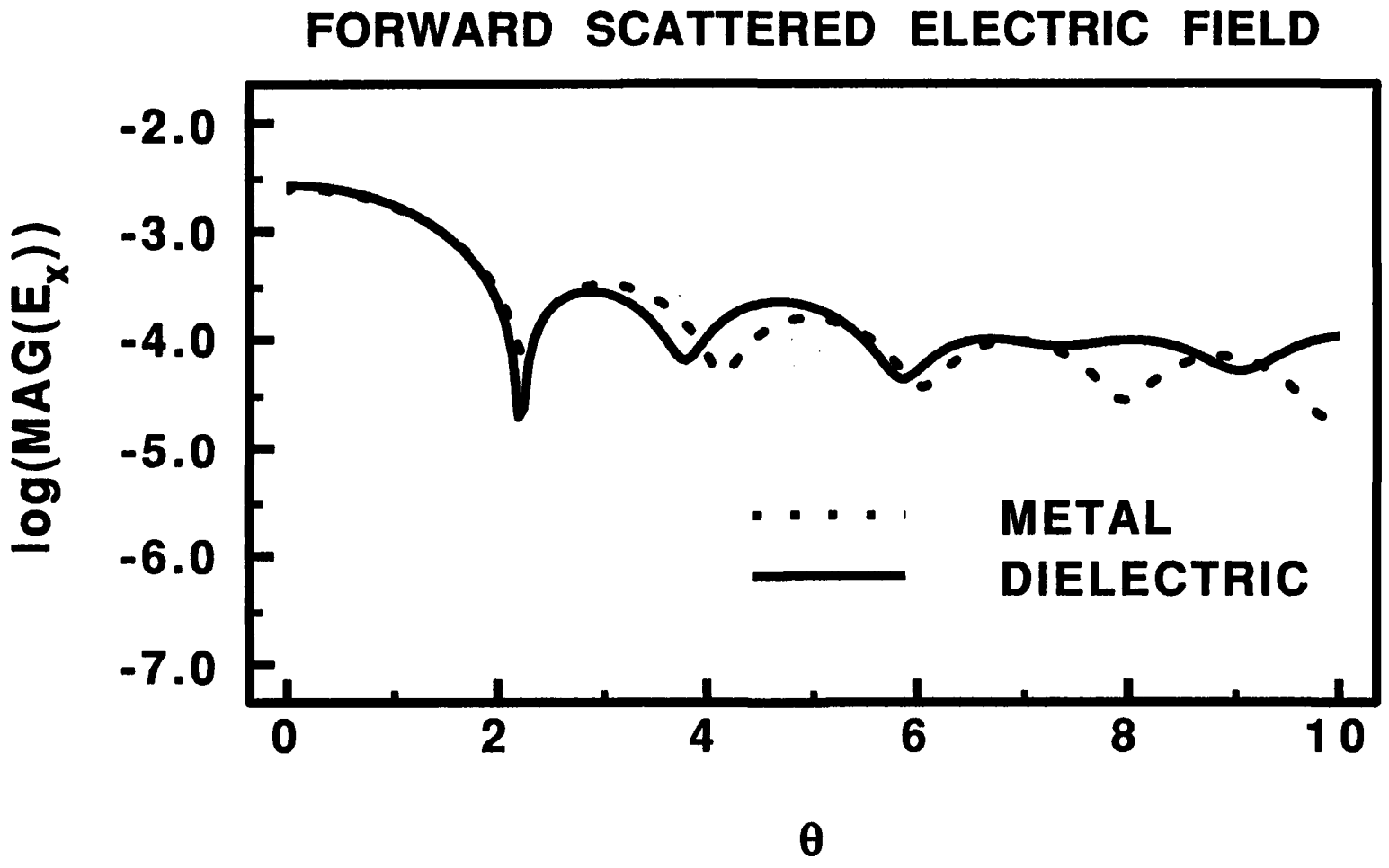

The similarity of the two previous curves in the near forward scattering region is emphasized in this plot where we show the log of the magnitude of the scattered field within the first 10°. Both curves show excellent agreement up to θ=5°.

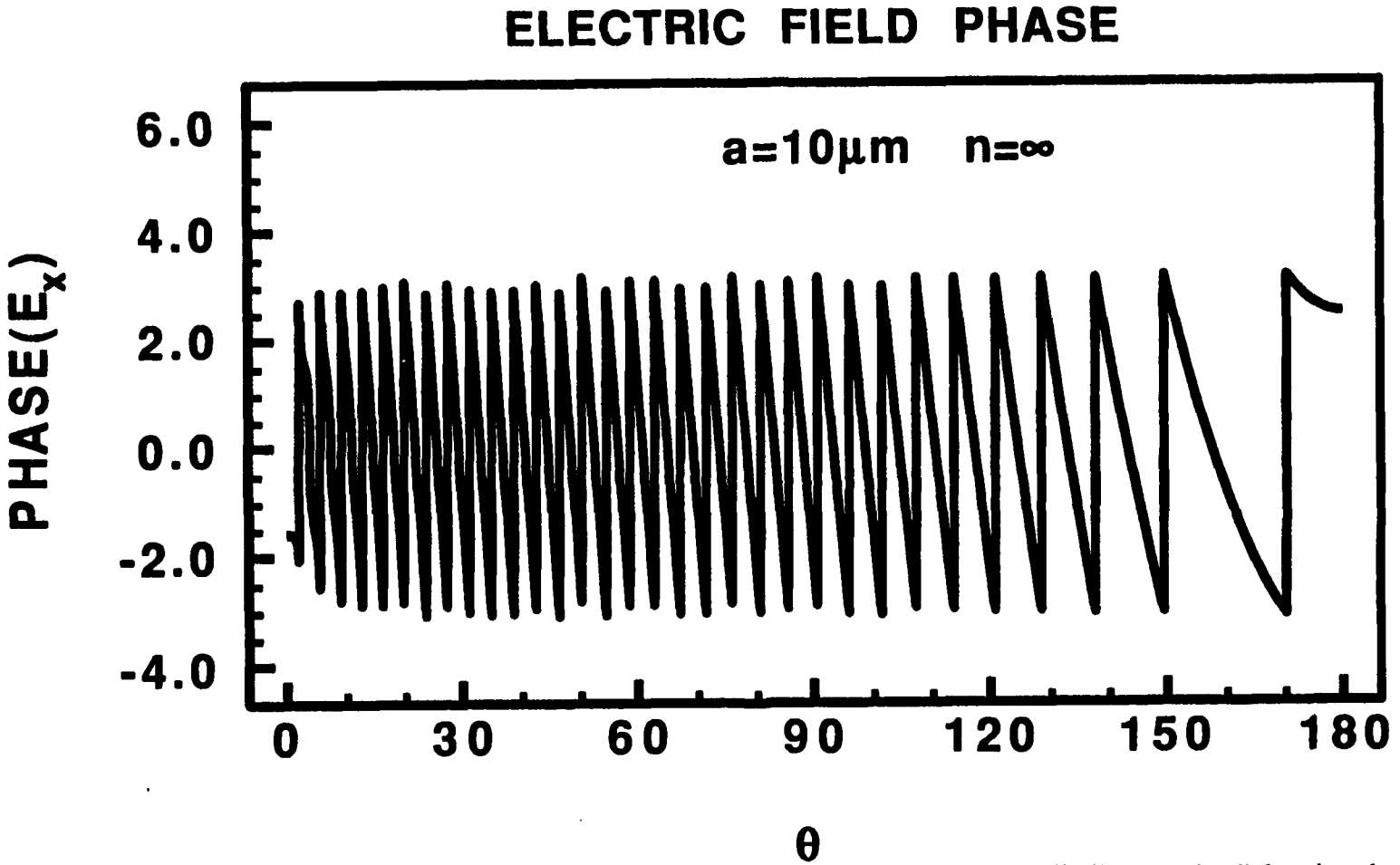

The phase of the scattered field, polarized in the x-direction, for a metal sphere is shown in this plot. Similarly to the dielectric sphere, the phase starts at approximately -1.7, decreases in value, and then oscillates between $-\pi$ and $+\pi$. Note, however, that unlike for the dielectric sphere, the phase for the metal sphere has a varying period, increasing as θ increases. From the magnitude and phase plots, we conclude that the near forward scattering region is a poor area to distinguish between a metal and dielectric sphere of equivalent size. However, the backscatter region is an excellent choice. This is because, in the backscatter region, the magnitude of the metal sphere is constant in values, while the magnitude for the dielectric sphere is highly oscillatory. The phases are also significantly different as previously discussed.

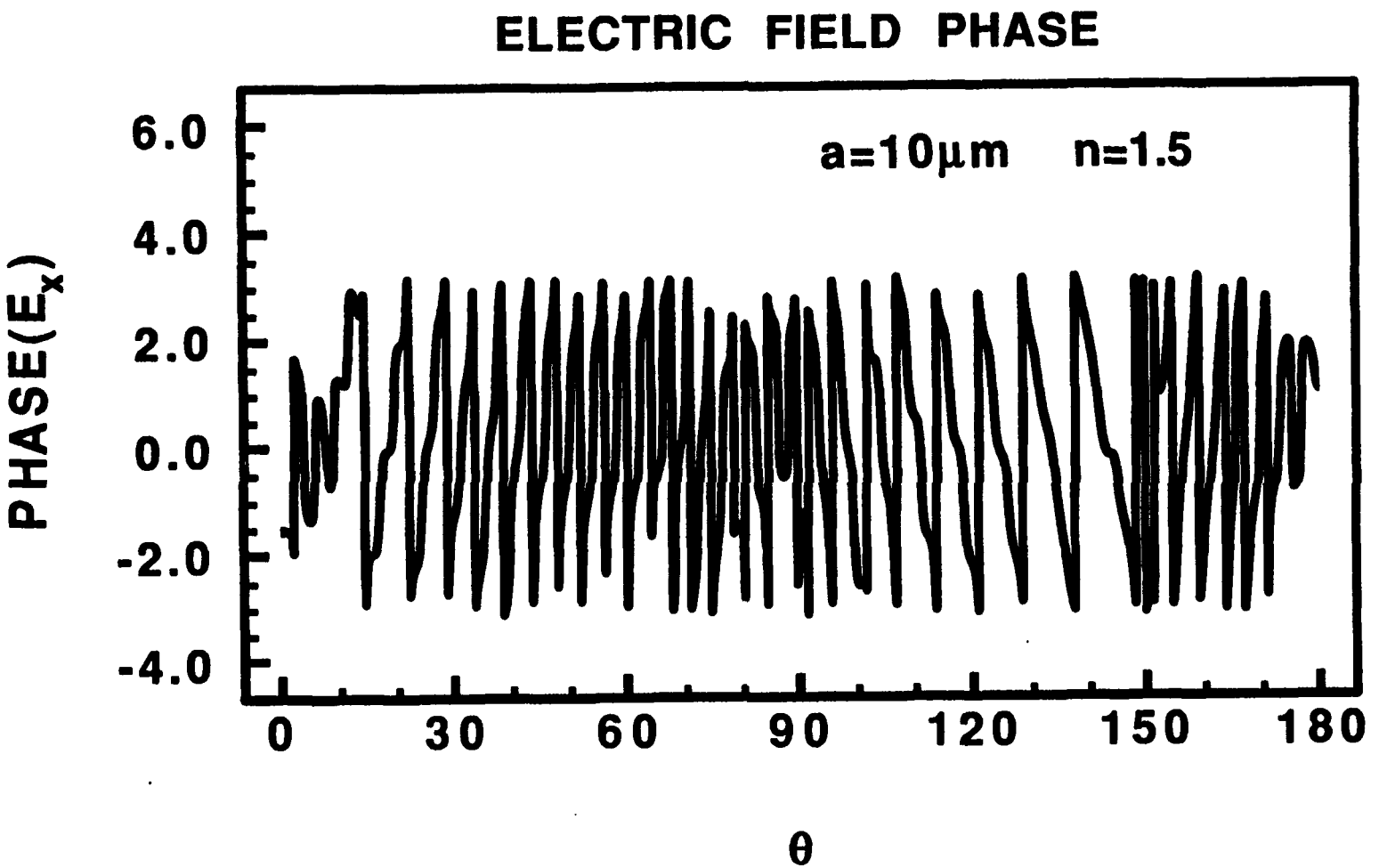

In this figure, we show the phase of the scattered field polarized in the x-direction for the dielectric sphere. The phase begins at approximately -1.7, decreases slightly, and then oscillates between $-\pi$ and $+\pi$. Note also the relatively constant period of the phase.

MAKING THE MATCHED FILTER

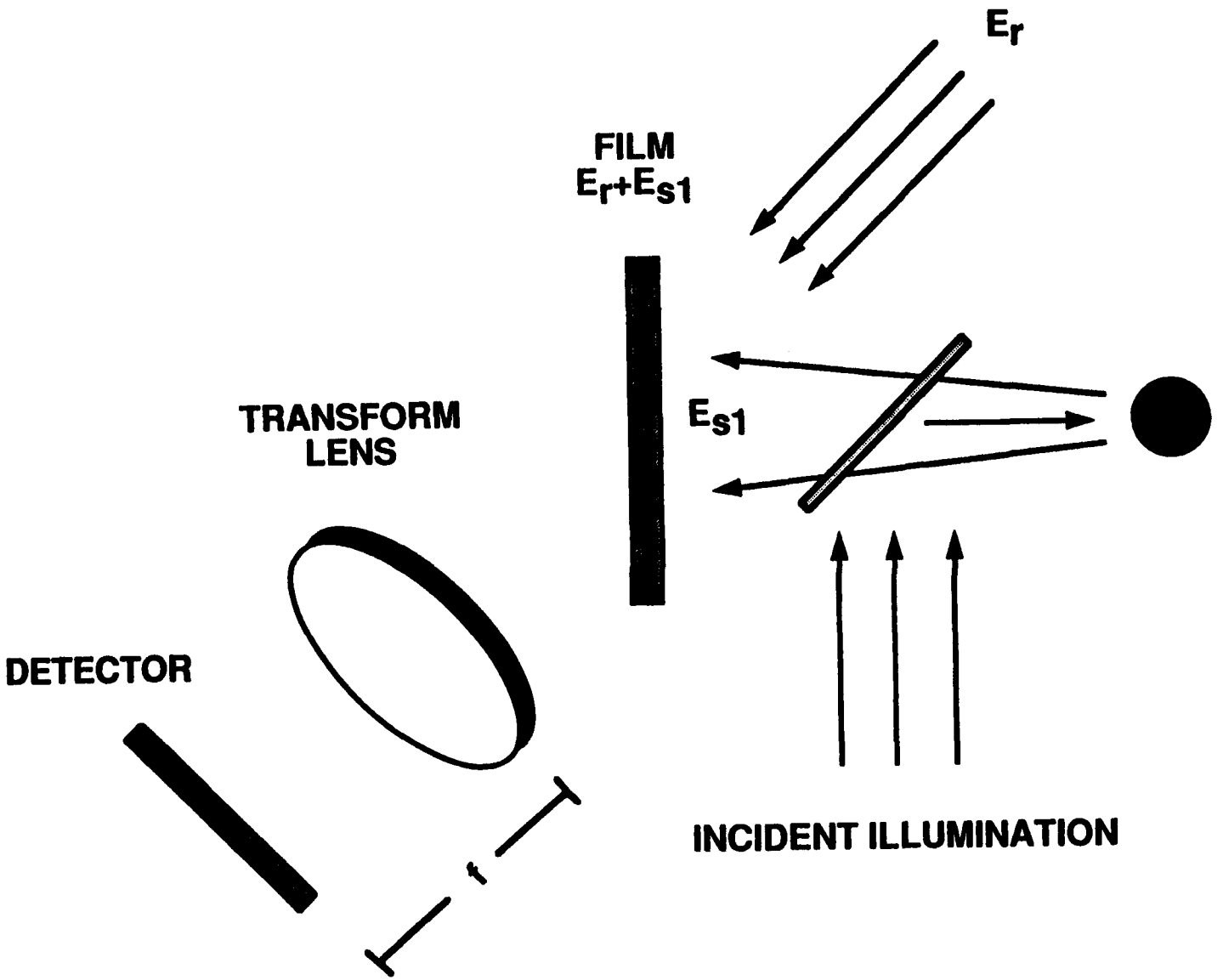

To include both the magnitude and phase of the backscattered scattered field in a sorting routine, we propose to use a matched filter. The construction of a matched filter is shown in this figure. The backscattered field, at the film location, is denoted by E_{s1}. A reference beam, propagating at an angle to the incident beam, is interfered with E_{s1}. The transform lens is used to produce, at the back focal plane, the optical transform pattern of the reference beam.

INTENSITY VALUE AT THE CORRELATION PLANE

Density Of Film

$$D = |E_{s1} + E_r|^2 = |E_{s1}|^2 + E_{s1}E_r^* + E_{s1}^* E_r + |E_r|^2$$

Output At Film

$$E_{s2}D = E_{s2}|E_{s1}|^2 + E_{s2}E_{s1}E_r^* + E_{s2}E_{s1}^* E_r + E_{s2}|E_r|^2$$

Intensity At Correlation Plane

$$I_{s1-s2} = \frac{1}{(\lambda f)^2}\left|\mathfrak{F}[E_{s1}] \otimes \mathfrak{F}[E_{s2}]\right|^2$$

Mathematically, the density, D, of the film after developing, will be given by the intensity of the two interfering beams, I. The third term in the expression for I constitutes the matched filter. If the reference beam is removed, and a second sphere with scattered field E_{s2} is examined, the output at the back side of the film will be given by $E_{s2}D$. The third term in the quantity $E_{s2}D$ is a reconstructed reference beam, modulated by the cross multiplication of the two scattered field, E_{s1} and E_{s2}. The transform lens will therefore produce the optical transform intensity of this quantity. The intensity of the optical transform pattern, at the correlation plane, is $I_{s1\text{-}s2}$. The symbol $\otimes$ represents a correlation and $\mathfrak{F}$ represent a Fourier transform.

BACKSCATTER

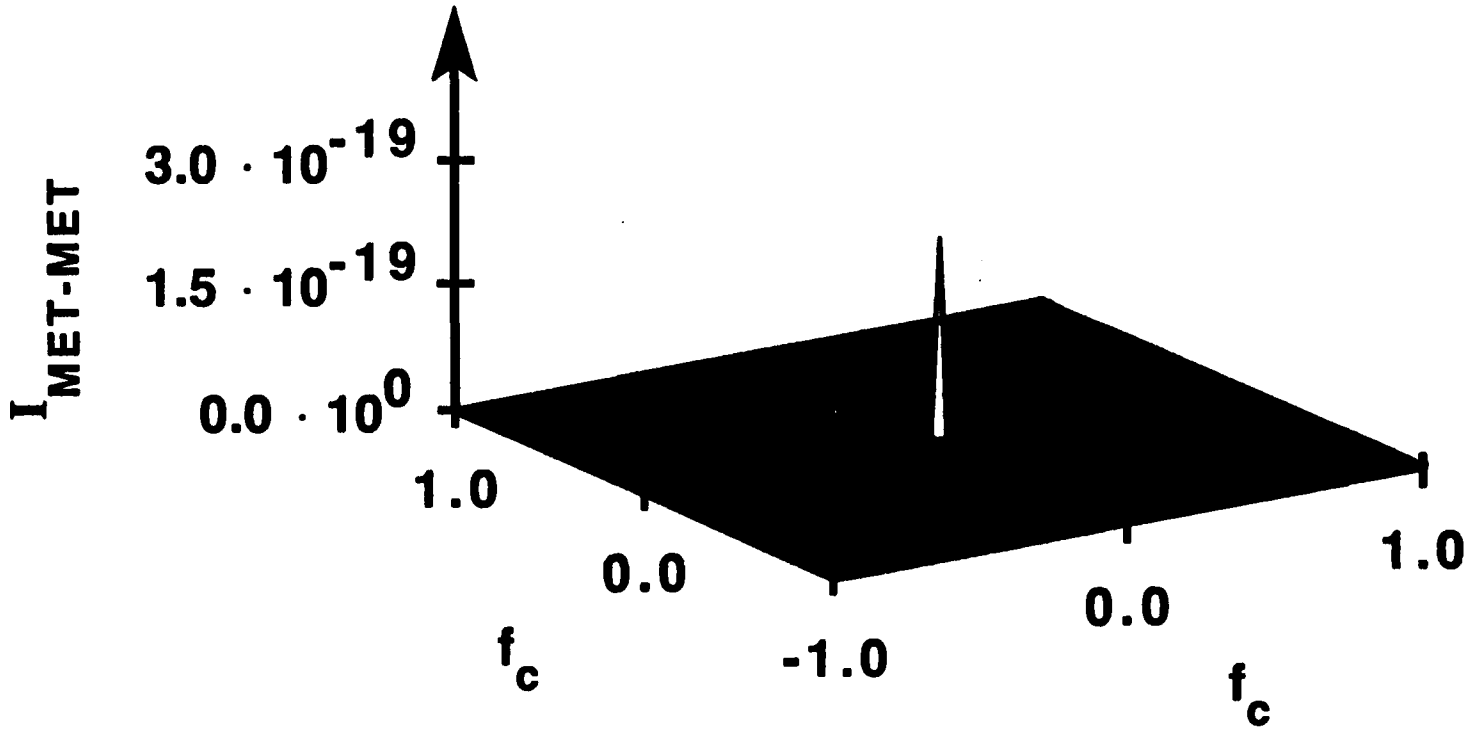

This plot shows $I_{MET-MET}$ using the backscattered field of a metal sphere versus the normalized transform frequency, f_c. Note the sharp peak at the center with no surrounding structure.

BACKSCATTER

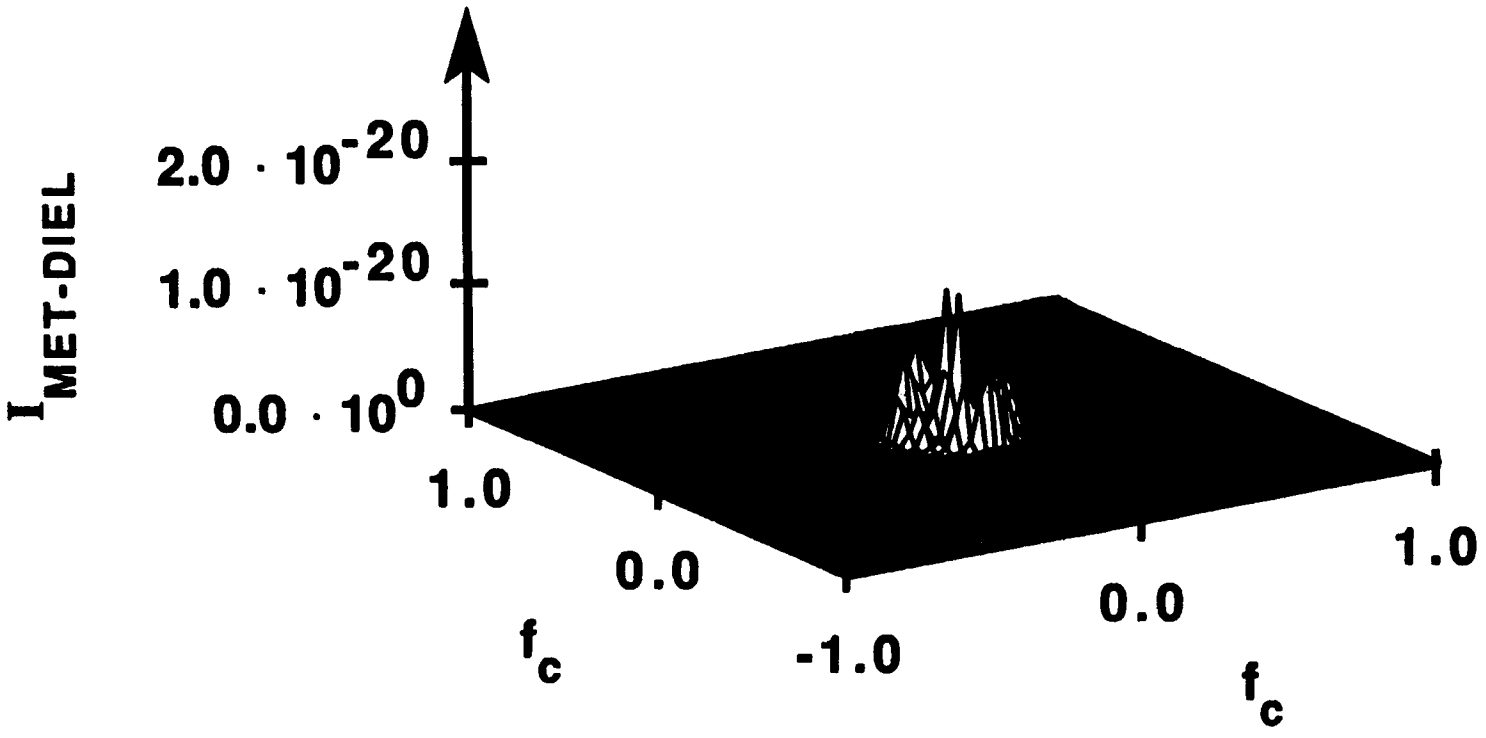

This plot shows $I_{MET-DIEL}$ using the backscattered fields of a metal and dielectric sphere versus the normalized transform frequency, f_c. Note that there is no central peak in the correlation intensity. Instead, there are multiple peaks over a wide frequency range. Sorting between the two particles is therefore possible by using a matched filter made with a metal sphere. A strong spike in the intensity at the correlation plane indicates a metal sphere, whereas jagged spikes represent a dielectric sphere.

BACKSCATTER

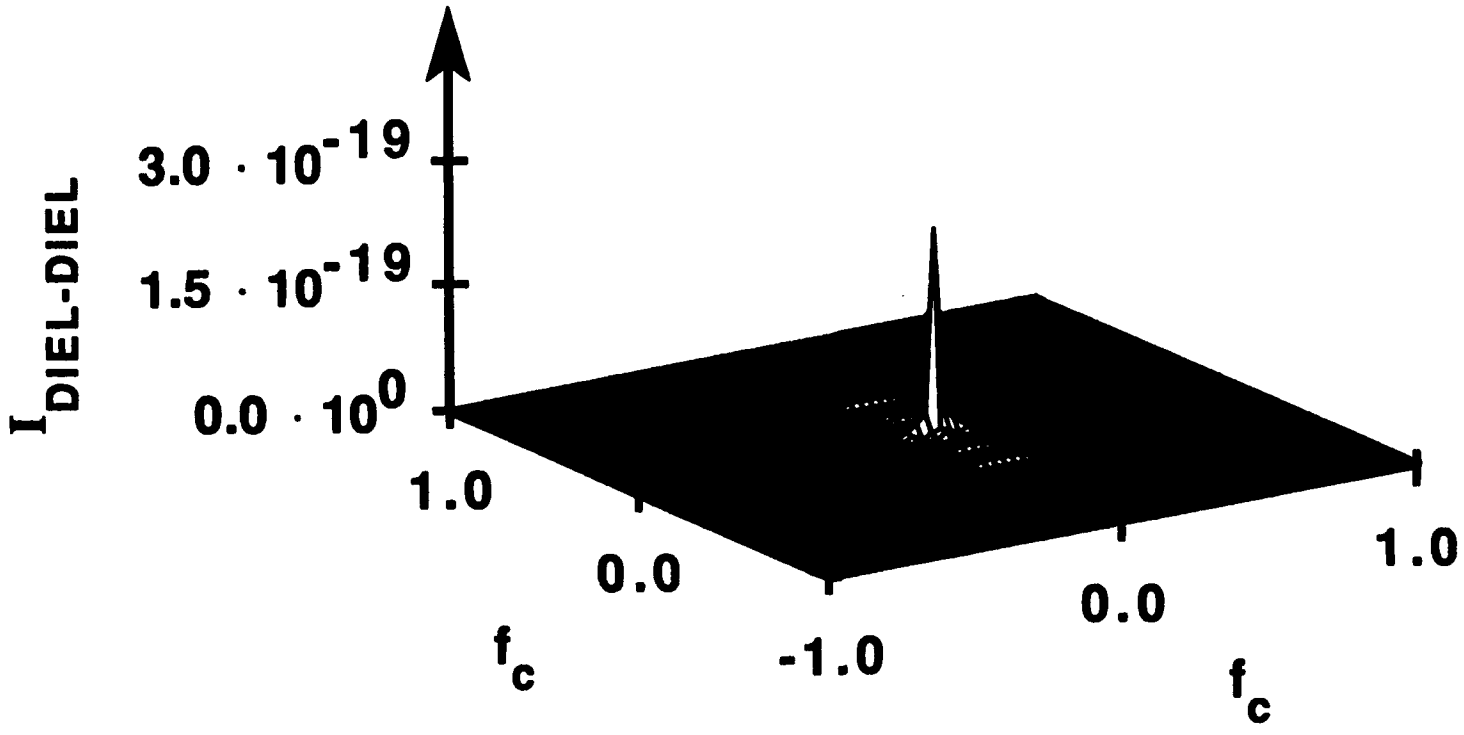

This plot shows $I_{DIEL-DIEL}$ using the backscattered field of a dielectric sphere versus the normalized transform frequency, f_c. As with the metal sphere previously, there is a sharp peak at the center. Therefore, the dielectric sphere can also be used to make the matched filter. Analysis of the intensity at the correlation plane is the same as for the matched filter made with the metal sphere.

CONCLUSIONS

- Sorting of two different particles (metal and dielectric) is possible.
- Characteristics in the correlation plane of a matched filter were used.
- The forward scattering region is not suitable for sorting.
- The backscatter region is excellent for sorting the particles.

RECOVERY OF PARTICULATE SIZE DISTRIBUTIONS BY INVERSION OF THE OPTICAL TRANSFORM PATTERN

RECOVERY OF PARTICLE SIZE DISTRIBUTIONS BY INVERSION OF THE OPTICAL TRANSFORM PATTERN

Scott D. Coston and Nicholas George

Institute of Optics
University of Rochester
Rochester, NY 14627

ABSTRACT

Experiments are presented for recovering the histograms of particle size from the optical transform intensity of spherical particles. We describe a novel inversion formula, and we provide computational details for obtaining particulate sizes from the transform intensity. The intensity is given by an integral over the size distribution multiplied by an Airy function (transform intensity for a single particle). The inversion formula is derived from the intensity using Bessel-delta identities and Abel transforms. By multiplying the intensity by an appropriate kernel and integrating over the diffraction angle, recovery of the particle size distribution is obtained. In the experiments, we use chrome masks with large numbers of tiny circular apertures or discs. These have been generated with three separate distributions: the gamma, the log-normal, and the bi-modal exponential. A discussion will be made of the calibration procedure for the ring-wedge detector as well as limitations due to particle size and number. Results using the inversion formula show excellent agreement with the known values of the size distributions.

RECOVERY OF PARTICLE SIZE DISTRIBUTION BY INVERSION OF THE OPTICAL TRANSFORM PATTERN†

Scott D. Coston

Nicholas George

The Institute of Optics

University of Rochester

1991

† Presnted at the 1991 Optical Society of America conference in San Jose.

STATEMENT OF THE PROBLEM

- **Find particle size distribution from the optical transform pattern.**
- **Require no prior information on the scatterers.**
- **Analyze resolution capabilities.**

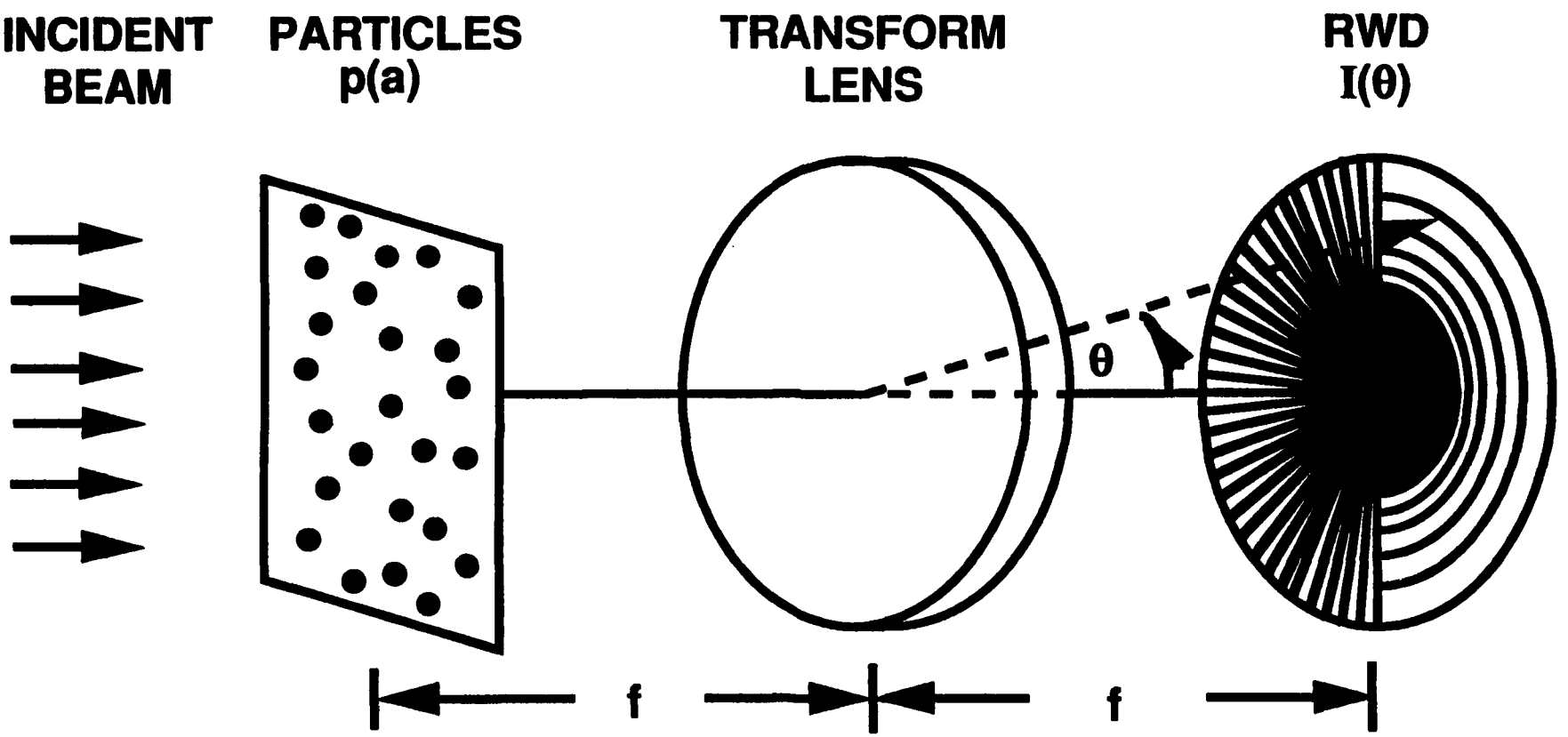

This figure shows the general geometry for recording the optical transform pattern for a collection of particles, incident on by a plane wave. The particles are described by the size distribution **p(a)**. The detector records the optical transform pattern of the particles, produced at the back focal plane of the transform lens. The scattering angle **θ** is measured from the optical axis to a point on the detector. The detector consist of 32 semi-angular rings and 32 wedges. However, since the transform pattern for a spherical particle is circularly symmetric, only the ring detectors are used.

DERIVATION OF THE INVERSION RESULT[†]

One can verify the identity:

$$p(a) = \frac{2\pi k^2}{a}\frac{d}{da}a\int_0^\infty p(a')a'^2\int_0^\infty \theta J_1^2(ka'\theta)J_1(ka\theta)Y_1(ka\theta)d\theta da'$$

Bessel identities and Abel transforms

$$I(\theta) = I_o\int_0^\infty p(a')a'^2\frac{J_1^2(ka'\theta)}{\theta^2 f^2}da'$$

$$p(a) = \frac{2\pi f^2 k^2}{a}\int_0^\infty \theta^3\frac{I(\theta)}{I_o}\frac{d}{da}\{aJ_1(ka\theta)Y_1(ka\theta)\}d\theta$$

† K. S. Shifrin and A. Y. Perleman, *Electromagnetic Scattering* (1967).
S. D. Coston and N. George, Appl. Opt. 30 (1991).

One can verify the identity recovering the function **p(a)** from an integral expression over the function **p(a')** by using Bessel identities and Abel transforms relationships. The quantities J_1 and Y_1 are Bessel functions of the first and second kind, respectively, of order one. The intensity recorded by the detector can be approximated by **I(θ)** which is an integral over the particle size distribution, **p(a)**, multiplied by the intensity of a single particle $I_o a^2 J_1^2(ka'\theta)/(\theta^2 f^2)$. Relating this intensity with the shown identity will result in the recovery of the particle size distribution, **p(a)**, from the intensity by an integral over the scattering angle, **θ**. Although that the integral is evaluated over an infinite scattering angle range, we cannot physically let **θ** go to infinity. Truncating the integral at a cut off angle, θ_{MAX} will cause a lost of information (resolution) in the inversion recovery. We now investigate this loss of information or resolution as a function of the cutoff angle.

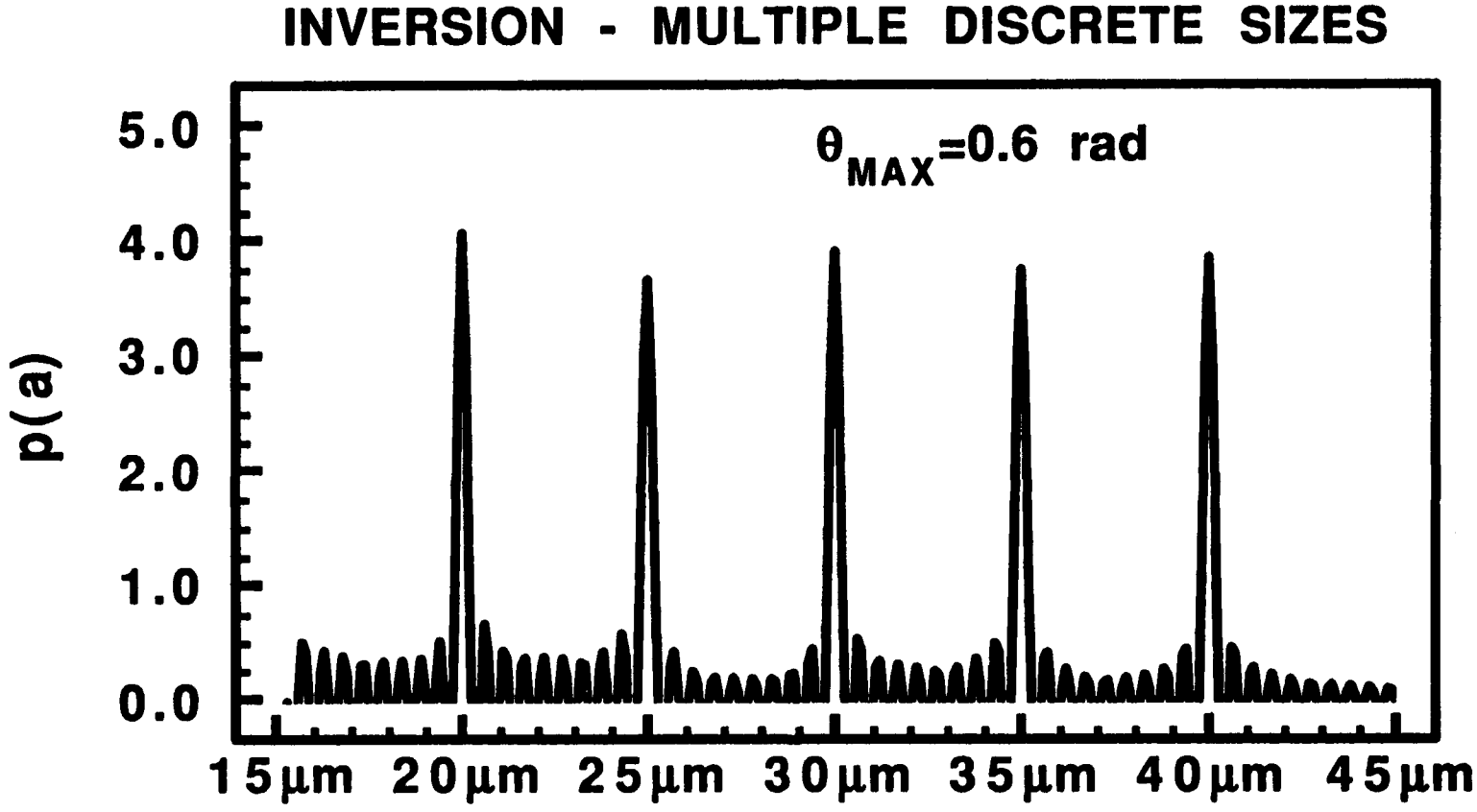

To examine the resolution of the inversion formula, we input for the distribution function a series of five discrete particle sizes. A perfect recovery of this distribution would be a series of Delta functions at the corresponding particle size location. However, due to the necessity of truncating the inversion integral at θ_{MAX}, there will not be a perfect recovery. Instead, there will be a peak of finite width at the particle size location. This is shown in this figure which is a plot of the recovered distribution versus particle radius, using θ_{MAX}=0.6 rads. Note that the spreading of each Delta function is independent of the particle size. It is only dependent on θ_{MAX}. The width of the recovered Delta function indicates the resolution. If we make a plot of the width at half maximum of the recovered delta functions versus θ_{MAX}, a resolution plot can be made.

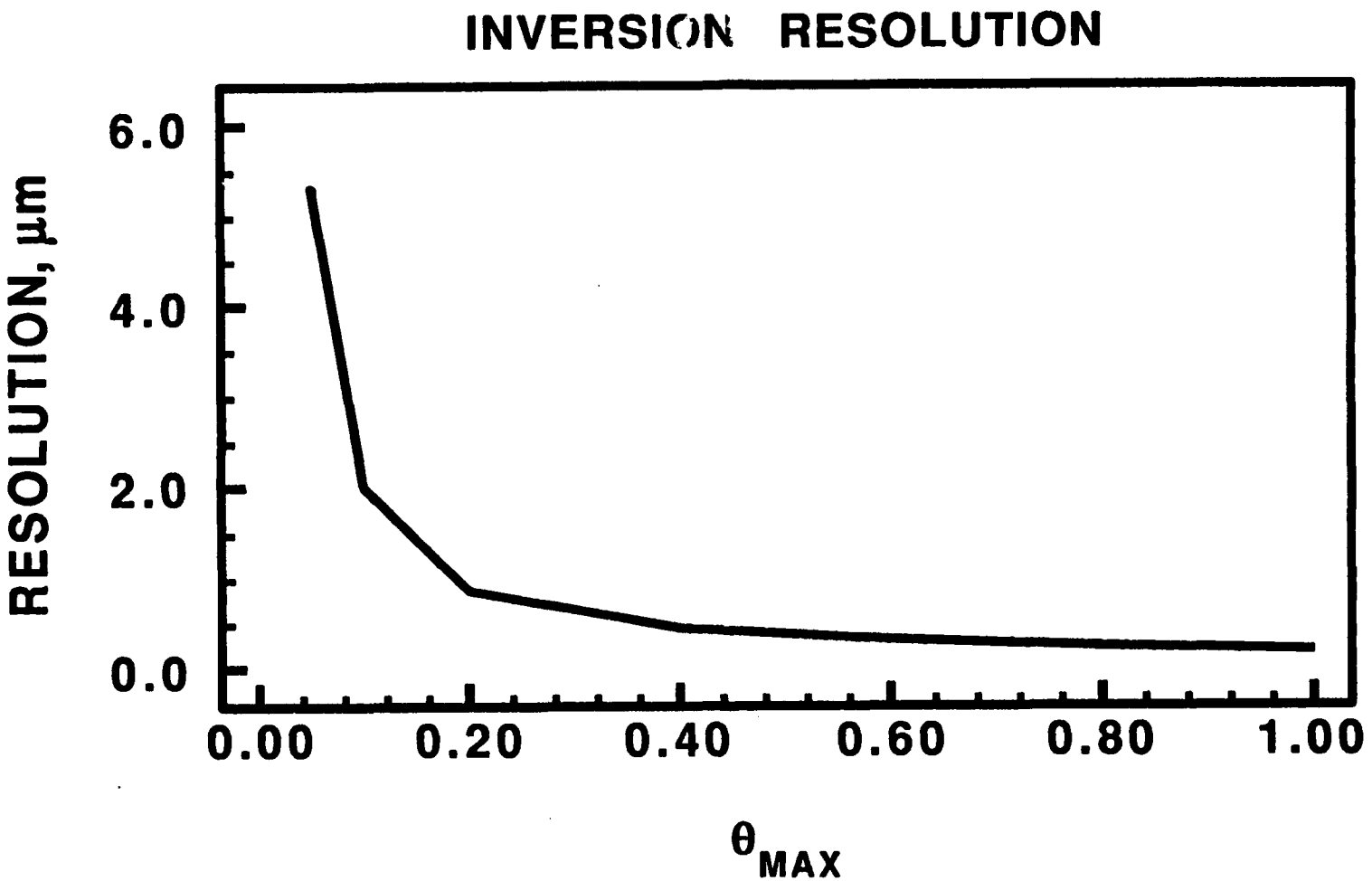

This resolution plot is shown in this graph. The general curve shows that the resolution is inversely proportional to θ_{MAX}. At values of $\theta_{MAX}<0.05$ rads, the resolution rapidly decreases, while for $\theta_{MAX}>0.4$ rads the resolution slowly increases. This indicates that the $0.05<\theta_{MAX}<0.4$ rads is the optimum cut off angle range. Below 0.05 too much resolution is loss, while above 0.4 rads little information is gained for the added computational time involved in calculating the inversion integral.

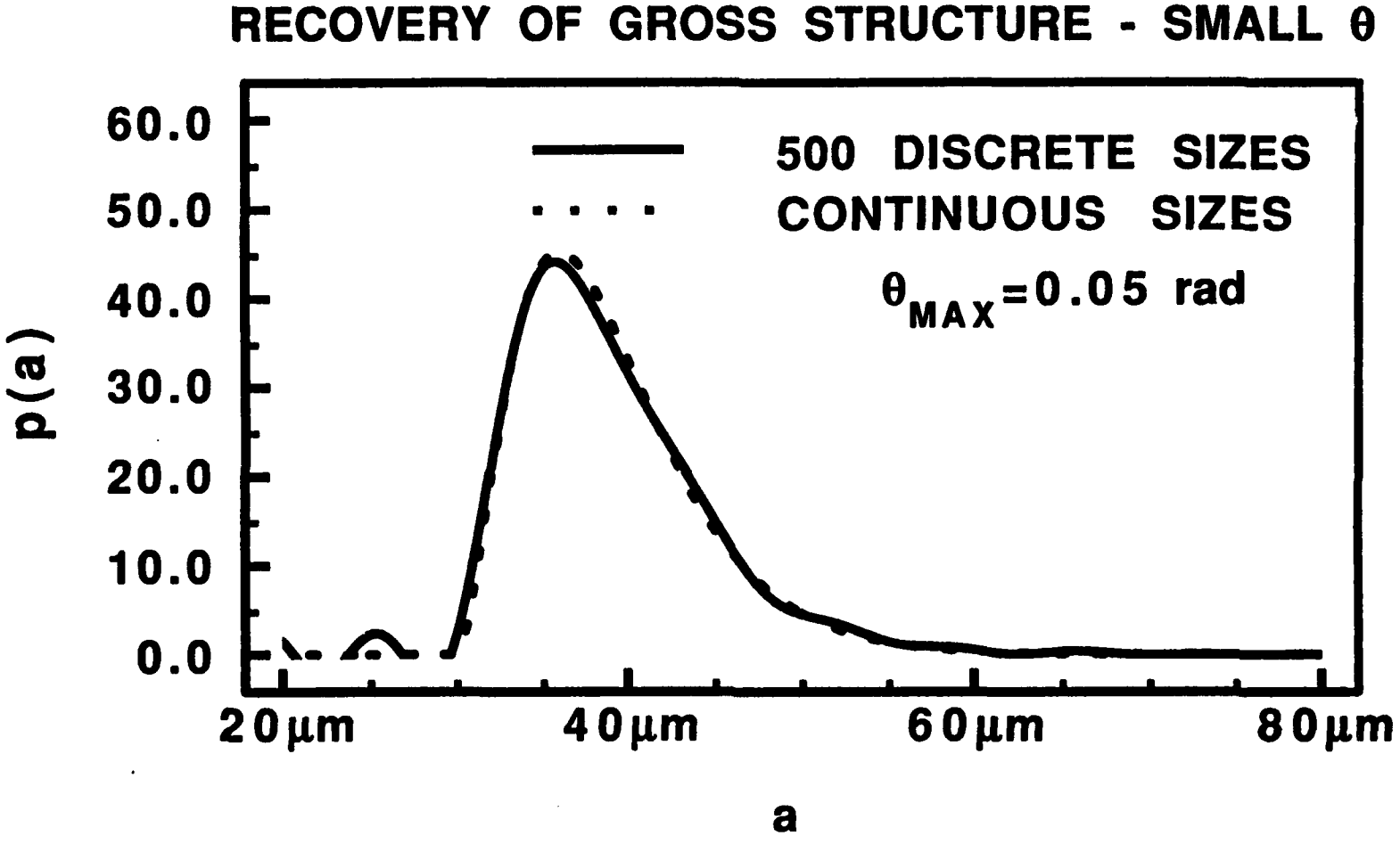

To verify the results in the resolution plot, we created a particle size distribution consisting of 500 discrete sizes. Using θ_{MAX}=0.05 rads (5.0 μm resolution), the resulting recovered distribution was calculated as shown in this plot. The ensemble average of this 500 discrete distribution is also plotted. Note the smooth nature of the recovered distributions. The following plots show the effects of increasing the value of θ_{MAX}.

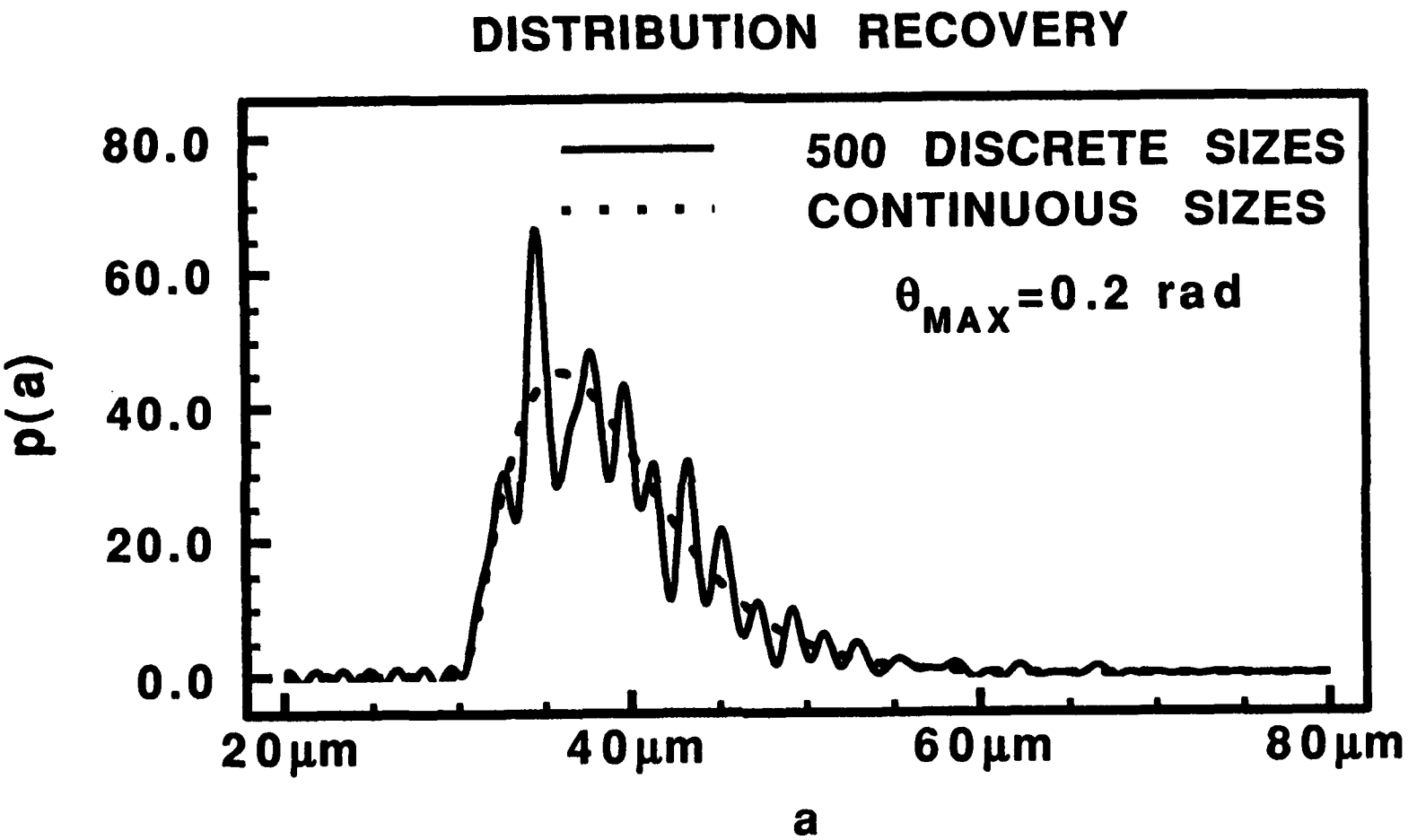

As before, but with θ_{MAX}=0.2 rads. The resolution is now 1.0 μm. Note the beginnings of some extra detail in the recovery.

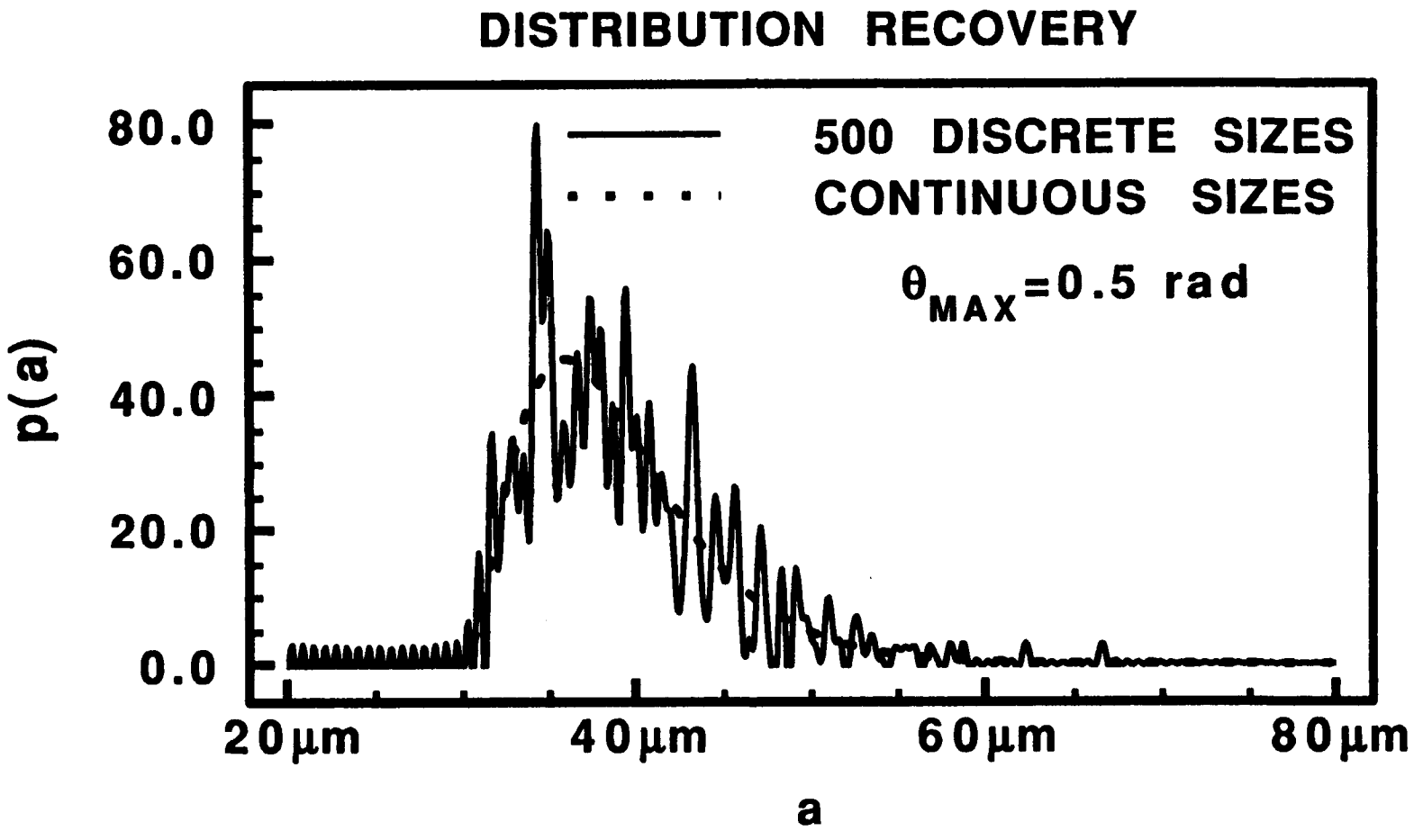

As before, but with θ_{MAX}=0.5 rads. The resolution is now 0.5 μm. There is now considerable fine structure detail in the recovered distribution.

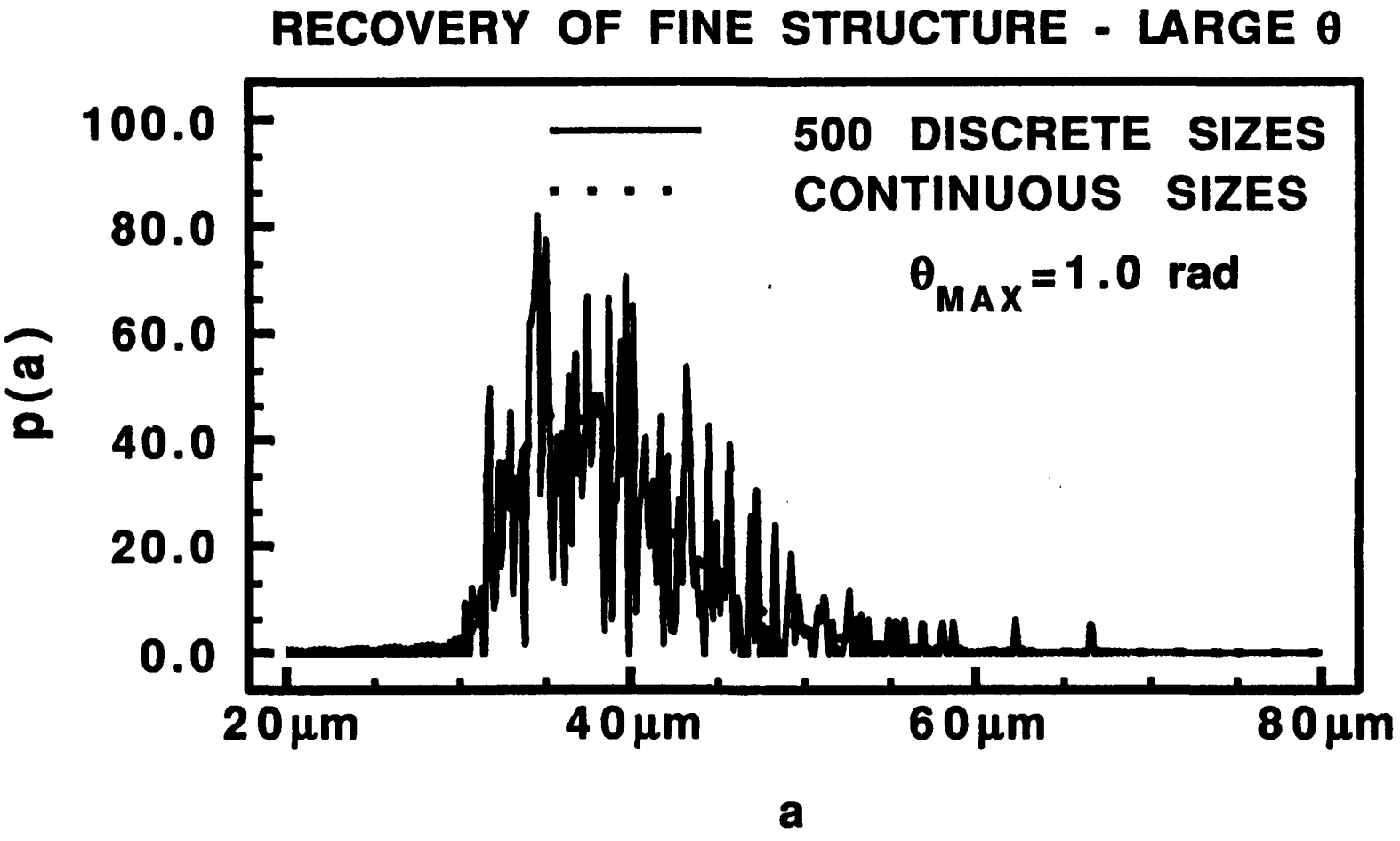

As before, but with θ_{MAX}=1.0 rads. The resolution is now 0.2 μm. Note the jagged appearance of the recovered distribution. These fine scale changes in the distribution represent the discrete nature of the particle size distribution. Examination of the actual particle sizes used to construct the distribution reveals that this fine scale structure should be present.

PARTICLE MASK

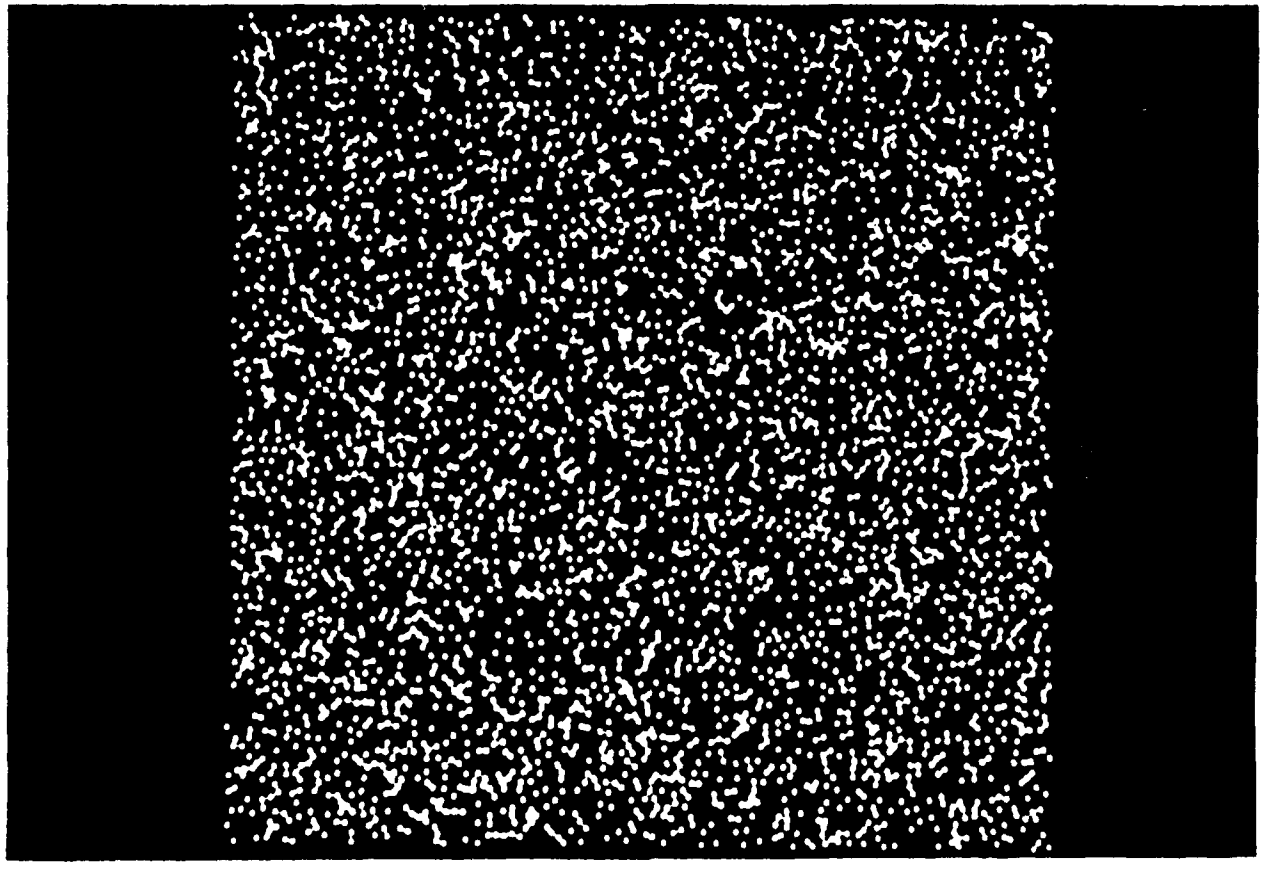

We now wish to show the results of some optical experiments using the inversion formula. For particle we constructed masks consisting of tiny aperture on a chrome coated glass slide and tiny chrome dots on a glass slide, using standard photolithographic techniques. This figures show one such example. The area containing the particles measures 2.5 mm square.

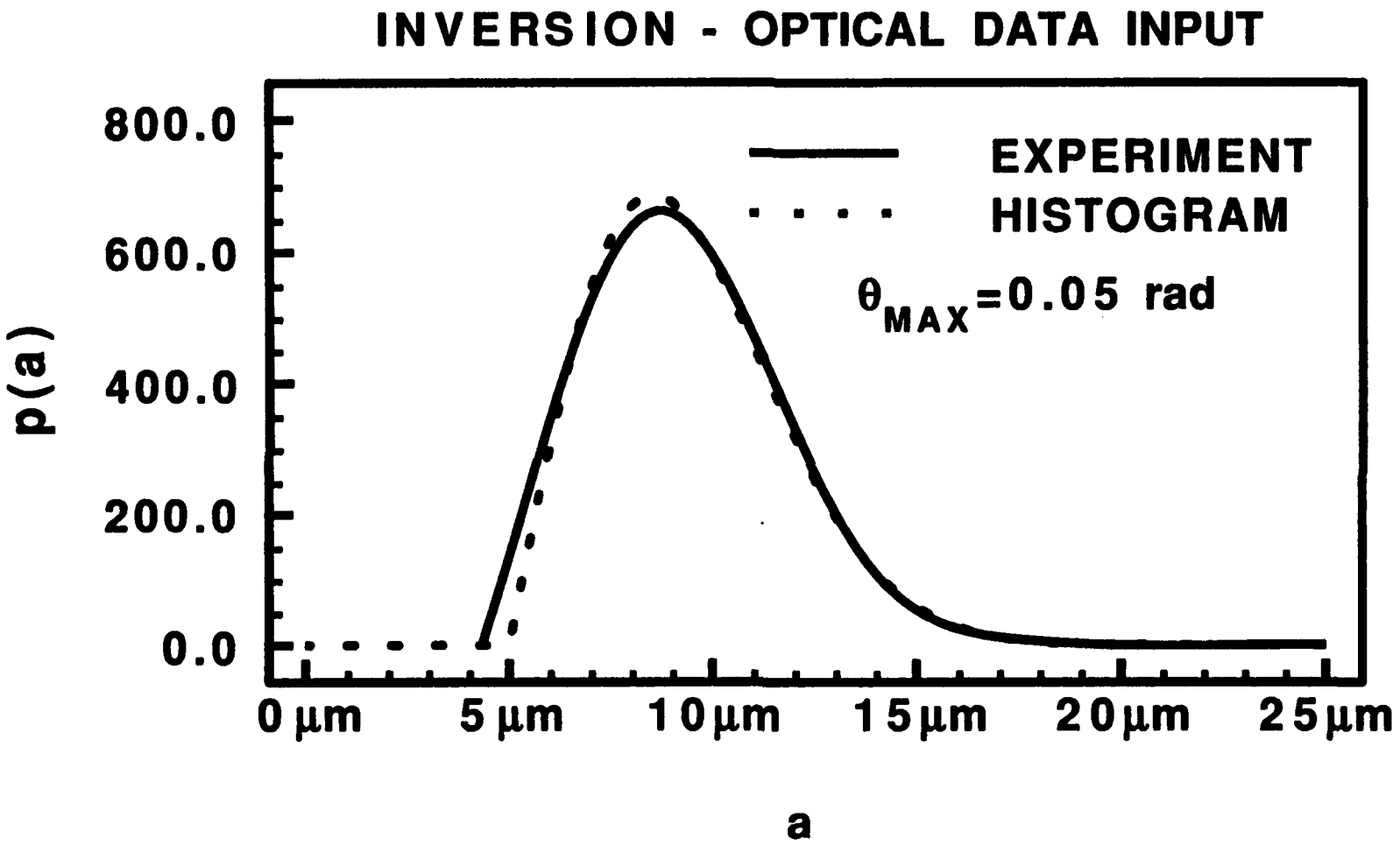

In the first experiment, we used a log-normal distribution consisting of 6000 particles. Using θ_{MAX}=0.05 radians, the recovered distribution versus particle size is shown in this plot. In addition, we show the ensemble average curve for the log-normal distribution. Note the excellent agreement between the two curves.

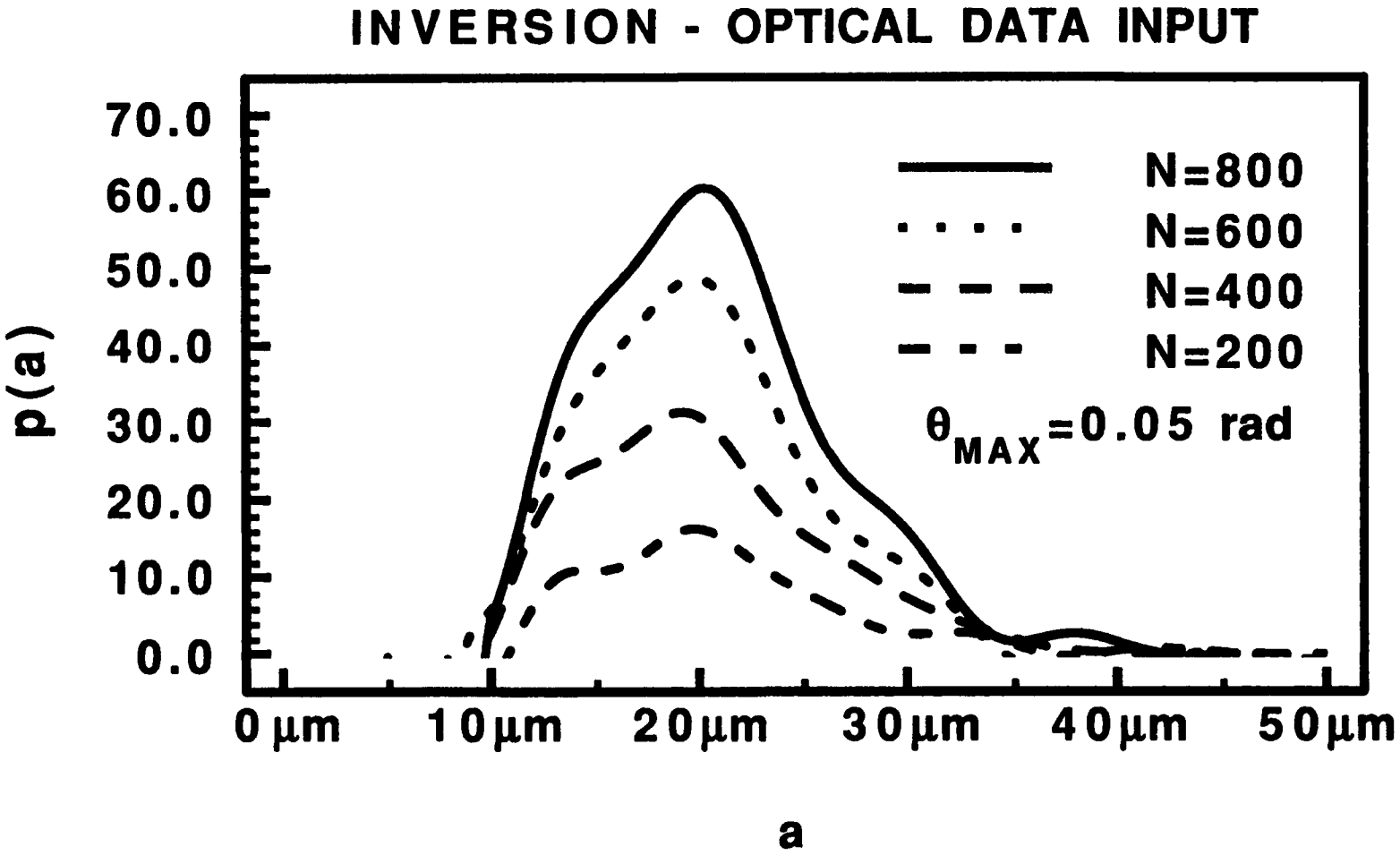

In a second experiment, we varied the number density of a log-normal distribution to confirm the linearity of the inversion formula. In this figure we plotted the recovered distributions versus particle size using θ_{MAX}=0.5 radians. Note the similarity of the four plot, differing only in the height.

INVERSION RESULTS

Known Value of N	Recovered Value of N
200	196
400	395
600	592
800	793

Here we show a comparison of the known particle numbers used in the previous figure, to number obtained by integrating the recovered distribution over all particle sizes. We see that there is excellent recovery of the particle number.

EVALUATION OF PHOTOLITHOGRAPHY

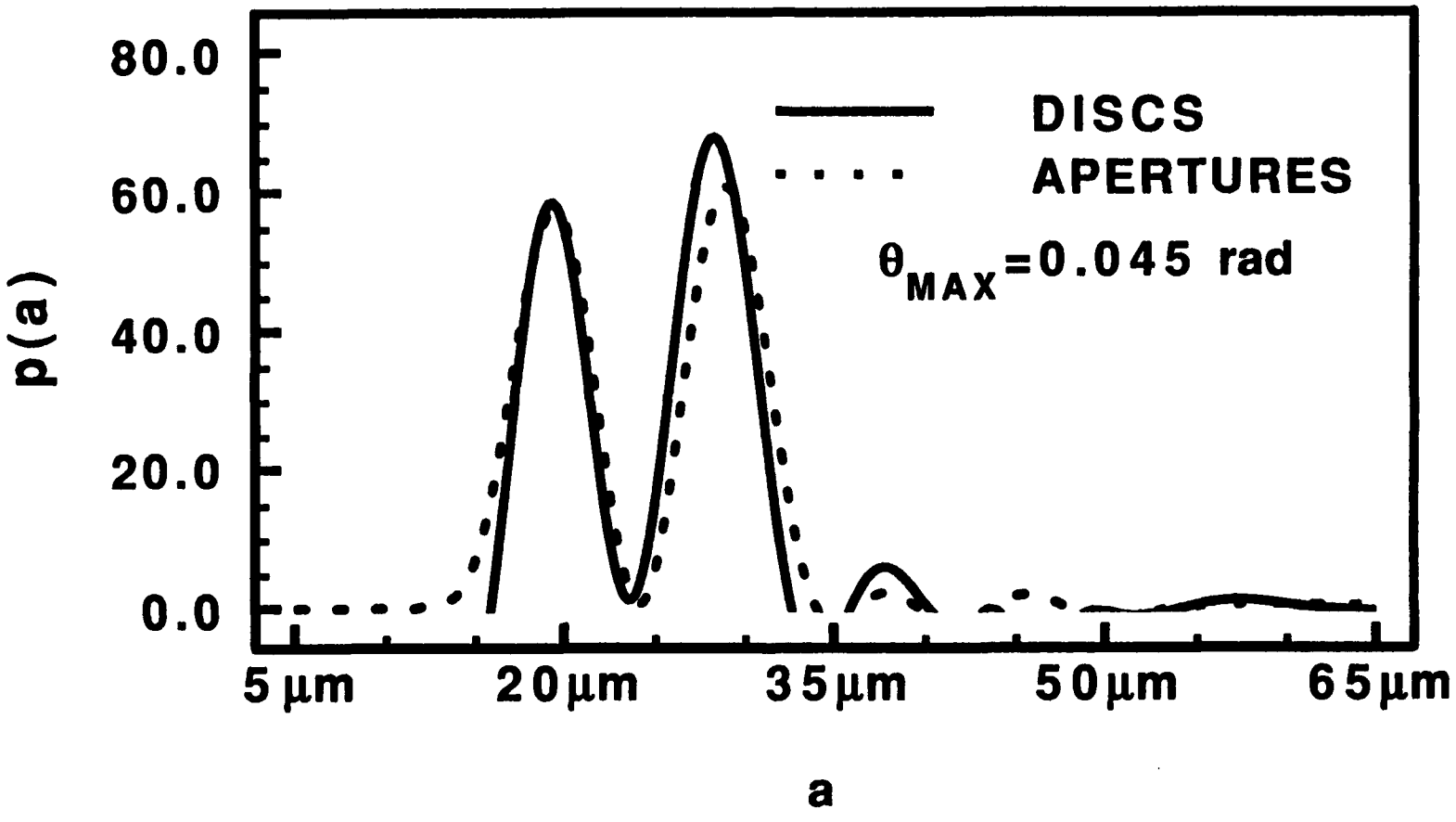

In a final experiment, we examined the ability to distinguish small changes in the particle size distribution. For this experiment, we made masks with apertures and chrome dots using the same original masters. However, due to variation in the construction process, slight differences in the sizes of the particles can be measured. Under microscopic examination, the discs were consistently 5% smaller in size than the corresponding apertures. In this plot we show the recovered distribution using the aperture and disc mask. The value of θ_{MAX}=0.045 radians was used. The discs are approximately 5% smaller in radii than the apertures.

CONCLUSIONS

- An inversion formula was presented for accurate recovery of particle size distributions from the optical transform pattern.
- Required no prior information on the scatterers.
- Resolution is inversely proportional to the maximum scattering angle and not dependent on the particle size.
- Can detect small variations in the particle size distribution.

BEAM SPLITTER CUBE FOR WHITE-LIGHT INTERFEROMETRY

BEAM SPLITTER CUBE FOR WHITE-LIGHT INTERFEROMETRY

Keith B. Farr and Nicholas George

Institute of Optics
University of Rochester
Rochester, NY 14627

ABSTRACT

We describe a technique for constructing beam splitter cubes in which we monitor the optical path difference with a wavelength tunable laser. A white-light interferometer should have path lengths equal to within $\lambda/4$. A larger path difference results in reduced fringe visibility and loss of signal-to-noise ratio. The beam splitter must be manufactured such that the two paths through glass are equal. We discuss the tolerance placed on the cube. One can assemble the cube from two right angle prisms in optical contact and in near-perfect alignment. Alternatively, we adjust the OPD to zero by sliding the prisms into proper alignment on a layer of uncured cement. Using a dye laser, we have readily achieved acceptable path differences. This method of measuring OPD with a tunable laser is shown to be useful for alignment of interferometers and measurement of aberrations in lens systems. A laser diode can be tuned by changing its operating current or temperature. We report results of optical path difference measurements using a laser diode.

Beam splitter cube for white-light interferometry †

Keith B. Farr
Nicholas George

University of Rochester
The Institute of Optics
Rochester, New York 14627

Presented at the 1991 Optical Society of America Conference
†This work was supported in part by the Army Research Office

Scope

- ***Tunable dye laser technique for controlling interferometer path differences to 0.25 or better.***
- ***Beam splitter cube with less than 1 μm path difference.***
- ***Achromatic interferometer***

Dye laser technique for measurement of interferometer path difference

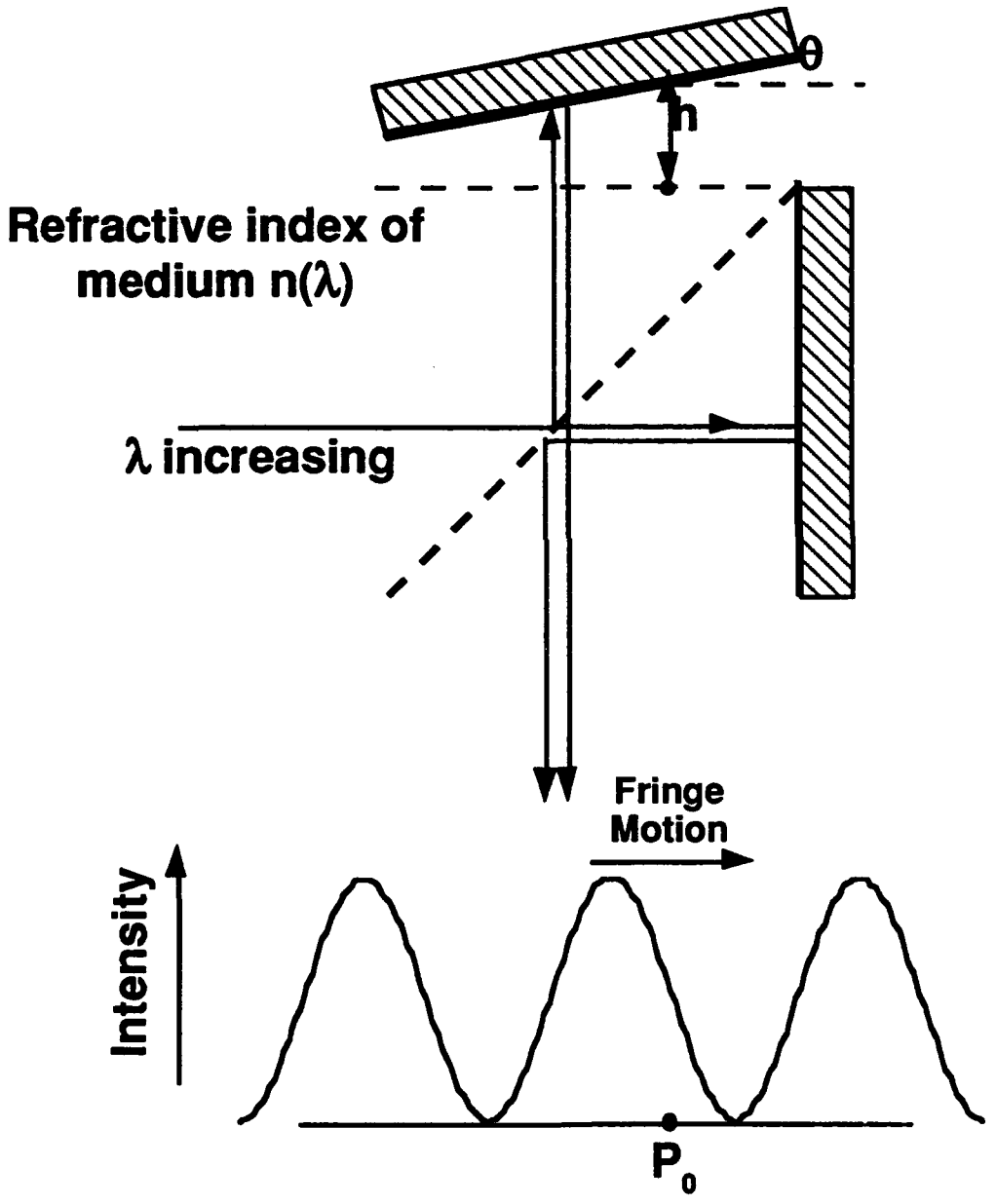

Calculation of path difference

Tunable wavelength laser illumination:

$$\lambda_0 - \frac{\Delta\lambda}{2} \le \lambda \le \lambda_0 + \frac{\Delta\lambda}{2}$$

Intensity at P_0:

$$I = \frac{1}{2} + \frac{1}{2}\cos\left[\frac{4\pi}{\lambda} n(\lambda) h\right]$$

Fringe count at P_0:

$$N = 2h\left[\frac{n\left(\lambda_0 - \frac{\Delta\lambda}{2}\right)}{\lambda_0 - \frac{\Delta\lambda}{2}} - \frac{n\left(\lambda_0 + \frac{\Delta\lambda}{2}\right)}{\lambda_0 + \frac{\Delta\lambda}{2}}\right]$$

$$\cong 2h\frac{\Delta\lambda}{\lambda_0^2} n_g(\lambda_0)$$

where $$n_g(\lambda) = n(\lambda) - \lambda\frac{dn}{d\lambda}$$

Beam splitter geometry

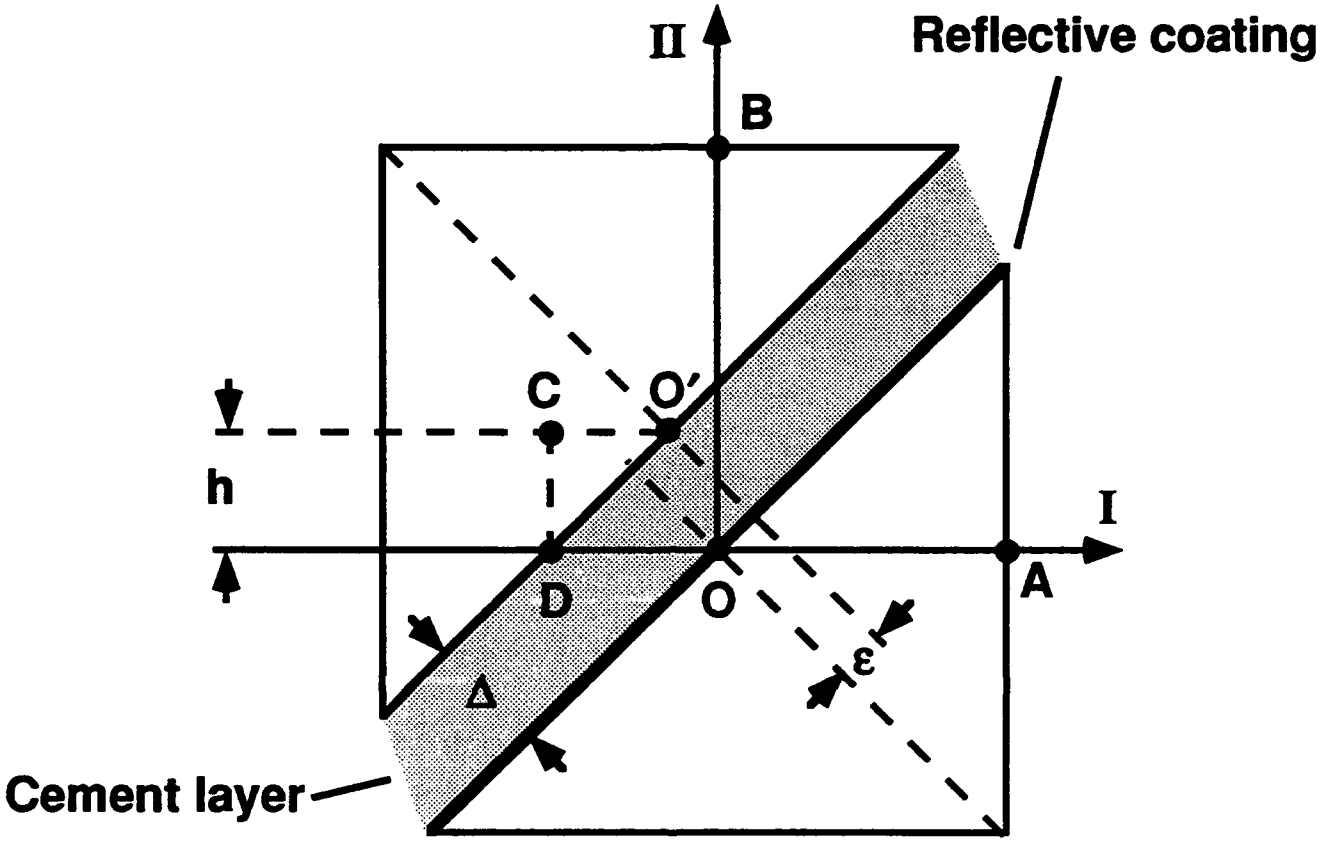

Extra geometrical length in path II:

$$h = \overline{OB} - \overline{OA} = \overline{CD}$$

By examination of triangle O'CD we find

$$h = \frac{\Delta + \varepsilon}{\sqrt{2}}$$

Beam splitter assembly

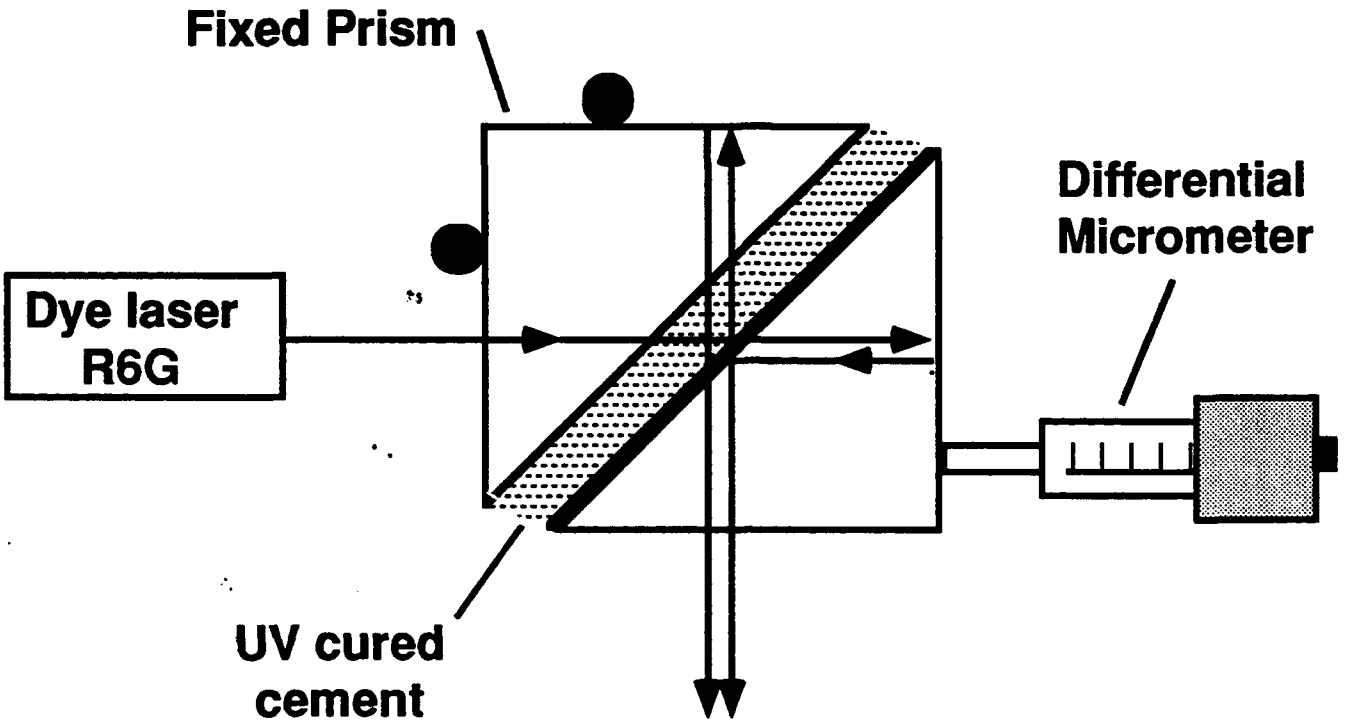

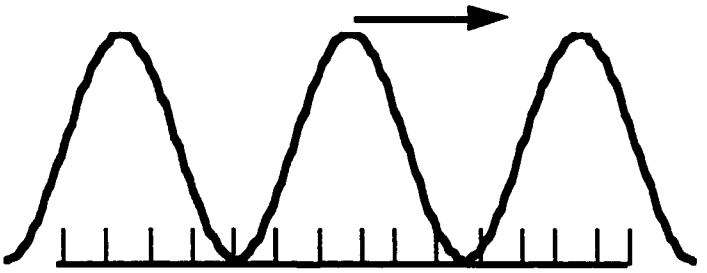

Fringes observed on a reticule

Visually measure: $N \sim \frac{1}{10}$ fringe

$h < 0.25\ \mu m$

Experimental Results
Beam splitter path difference measurements

		Fringe Count, N		Calculated Path Difference, p	
		Forward	Reverse	Forward	Reverse
Commercial beam splitters	A	20.6	33.2	98.8 μm	159.2 μm
	B	21.4	28.8	102.6	138.1
	C	3.5	9.0	16.8	43.2
Optical contact beam splitter	D	75.0	77.5	359.6	371.6
White-light beam splitters	E	0.25	11.2	1.2	53.7
	F	0.25	—	1.2	—

Forward

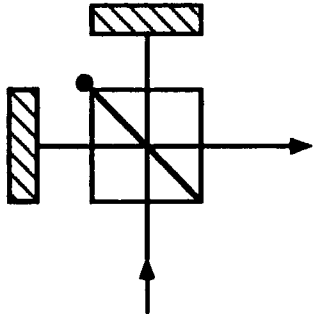

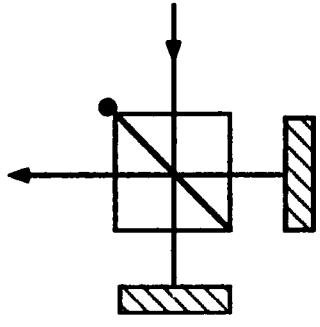

Reverse

White-light interferometry:

Spatial transform system

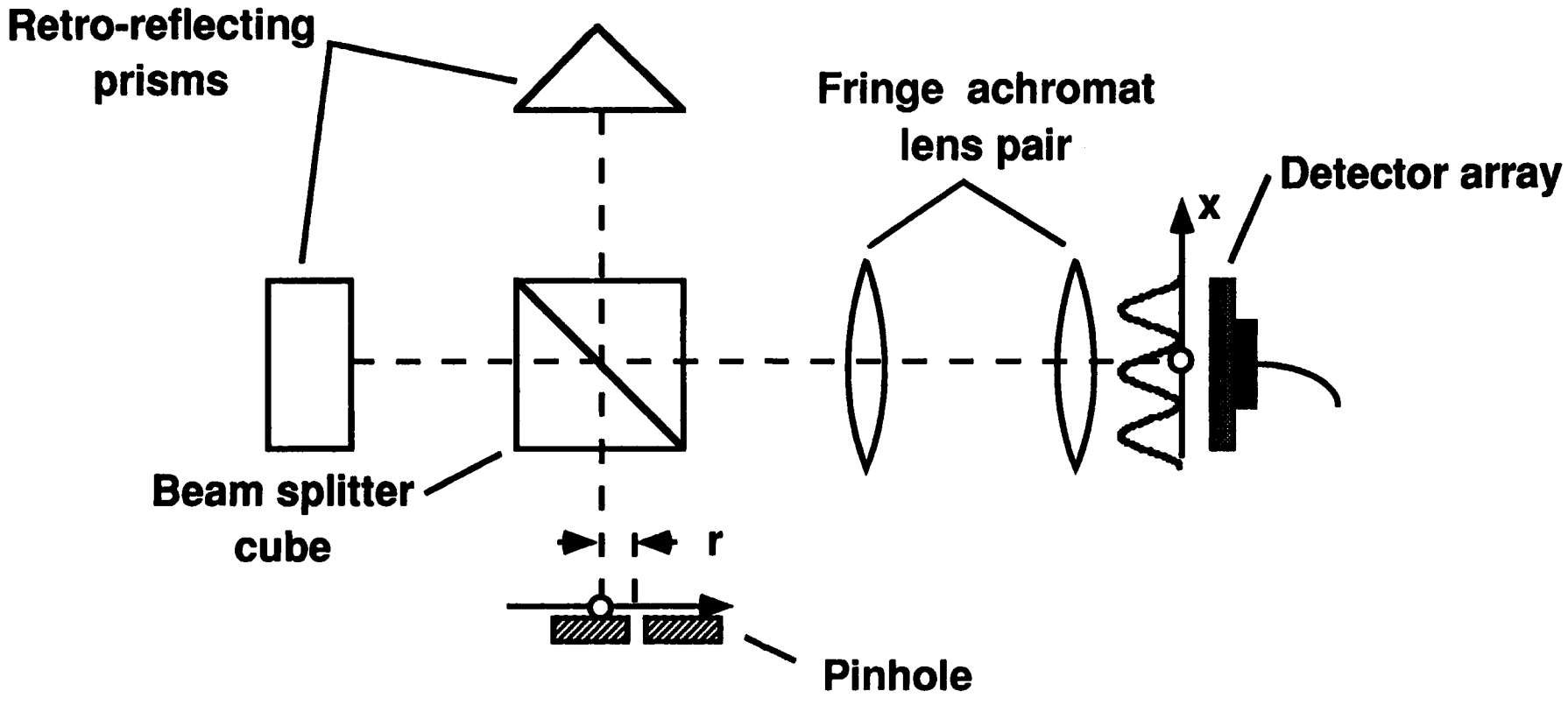

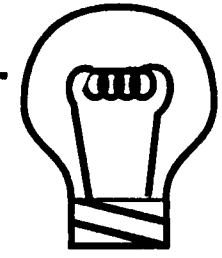

$$\lambda_0 - \frac{\Delta\lambda}{2} \le \lambda \le \lambda_0 + \frac{\Delta\lambda}{2}$$

If interferometer paths are equal

$$I = \frac{1}{2} + \frac{1}{2}\cos 4\pi Drx$$

Summary

- ***OPD < 0.25 μm***
  - ***Tunable dye laser -- fringe counting***
  - ***Tunable diode laser -- electronic detection***
- ***Beam splitter cube***
  - ***White light interferometry***
- ***Achromatic interferometer***
  - ***White-light cosine transform***
  - ***Beam splitter path difference ~ 1 to 10 μm***
  - ***Alignment by dye laser***

Fig. 1 The path difference h in a two-beam interferometer can be measured using a wavelength-tunable laser. A tilt θ is introduced to cause a spatial fringe pattern to be formed.

Fig. 2 When the wavelength is increased the phase decreases monotonically causing the fringes to move. With each 2π phase change the pattern moves one fringe width. The fringe count is proportional to the geometrical path difference h.

Fig. 3 A beam splitter cube is constructed of two identical right angle prisms. If they are placed into contact to form a perfect cube then the path difference will be zero. Two possible misalignment are a cement layer of thickness Δ and slide misalignment ε defined by the distance between the altitudes of the two prisms. Even if a cement layer is used one can always find a position at which the path difference is zero.

Fig. 4 The beam splitter cube is assembled under interferometric control. Two prisms are assembled with a layer of uncured cement and placed into a special jig which fixes one prism while allowing the other to be moved by a differential micrometer. A dye laser illuminates the cube and an interference pattern is formed by the light reflected from the cube faces. As the laser wavelength increases the fringe pattern moves and the fringes are counted. The prisms are then slid into a position where the fringes are stationary. At this point the path difference is zero. The cement is set using an ultraviolet lamp.

Fig. 5 Experimental results of path difference measurements of several beam splitters.

Fig 6. The spatial transform system is an example of a white-light interferometer. The pinhole located a distance h from the optic axis is illuminated by a source of bandwidth $\Delta\lambda$ centered at λ_0. The interferometer consists of a beamsplitter and two right-angle prisms tuned at 90^0 with respect to each other. With this arrangement the point source at h appears as two point sources separated by 2h and which interfere coherently. The fringe achromat is designed such that the fringes at the detector do not change with wavelength. For this reason the spatial transform system is particularly good for measurements of visibility. Such an interferometer requires that the path difference in the beamsplitter be from 1 to 10 μm.

BACKSCATTER FROM A TILTED ROUGH DISC

BACKSCATTER FROM A TILTED ROUGH DISC

Donald J. Schertler and Nicholas George

Institute of Optics
University of Rochester
Rochester, NY 14627

ABSTRACT

We present theoretical and experimental results for the backscattered intensity from a roughened metallic disc tilted at an arbitrary angle to the incident illumination. As the rms roughness is increased from 1μm to 10μm the zero-tilt intensity decreases by more than 1000 but at a 75° tilt it is shown to increase by more than 100. We also investigate the decorrelation of speckle with wavelength at various tilt angles. Tilting the surface to the illumination and then observing the intensity pattern in the specular direction gives a means of characterizing the roughness parameters. In performing the calculation the effect of shadowing must be included. We analyze this effect by comparing the calculated results with shadowing to those without shadowing. The effect becomes significant for moderate tilt angles (>60°) and large roughness. In addition we review recent developments in enhanced backscatter as applied to rough surfaces. Several techniques for producing the roughened surfaces are also described including: (1) beadblasting, (2) photolithography/ion-etching and (3) exposing of photo-resist to controlled speckle patterns. These techniques give us the ability to produce surfaces with rms roughnesses ranging from 1μm to 10μm and correlation lengths from 1μm to 50μm.

Backscatter from a Tilted, Roughened Disc†

Donald J. Schertler

Nicholas George

Institute of Optics
University of Rochester

†This research is supported by the US Army Research Office.
Presented at the Annual meeting of the Optical Society of America, November, 1991.

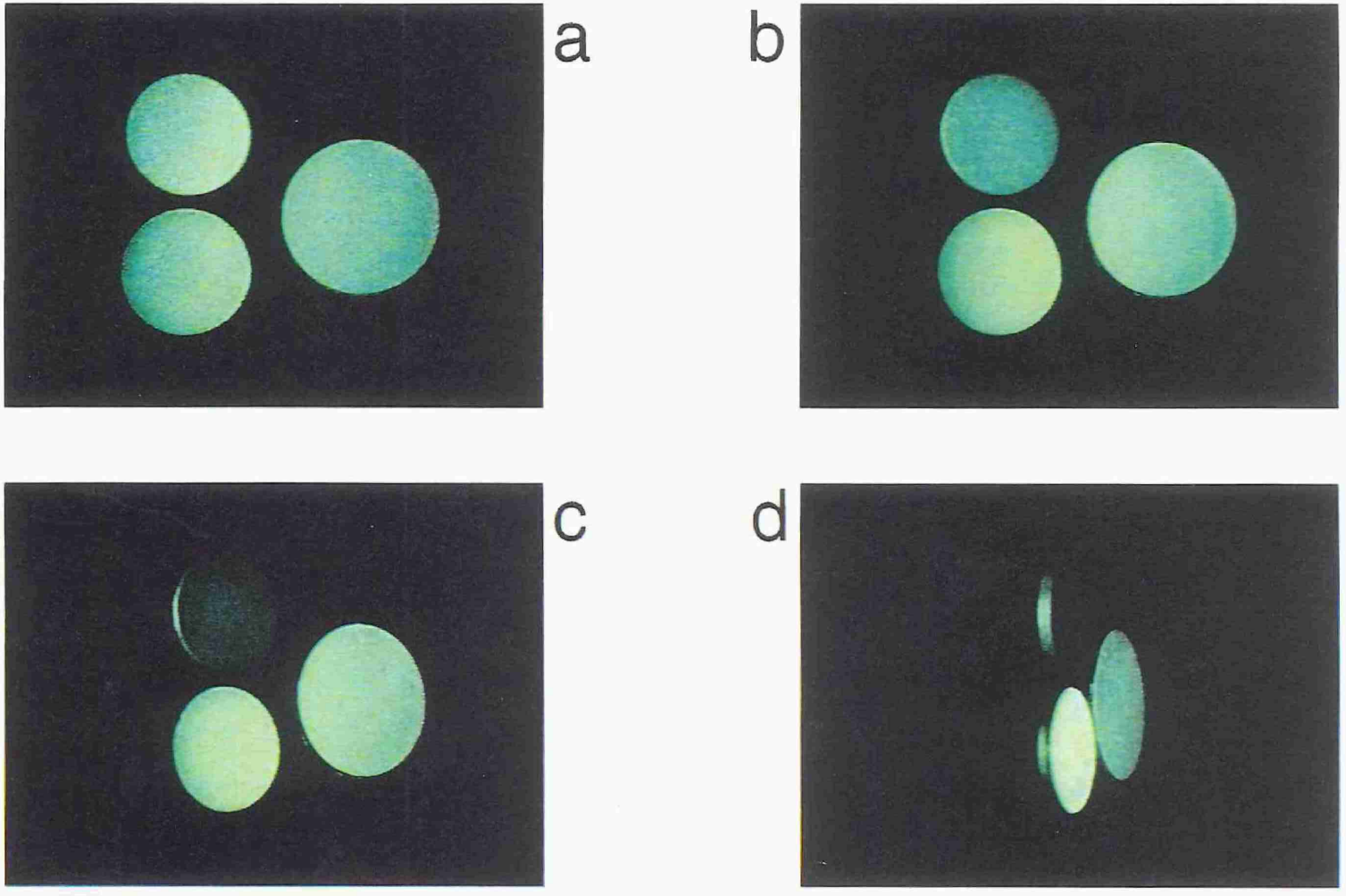

Page 2. Rotating Discs

This series of pictures illustrates the problem. Shown are three discs tilted at various angles to the illumination. The discs are viewed through a beam splitter so that we see the direct backscatter. The tilt angles are a) zero degrees, b) 20°, c) 40° and d) 70°. The large disc has a diffuse white surface. The smaller two are one inch diameter silver discs that have been roughened: the upper left at 2μm rms roughness using a bead-blasting process, and the lower at 8μm using an ion-beam etching of a speckle pattern exposed in photo-resist. As the discs are tilted the 2μm disc scatters less and less toward the illuminating direction while the 8μm and diffuse white discs continue scattering strongly. At 70° the 8μm disc is now considerably brighter than the other two. This is explained in terms of the roughness parameters of the discs.

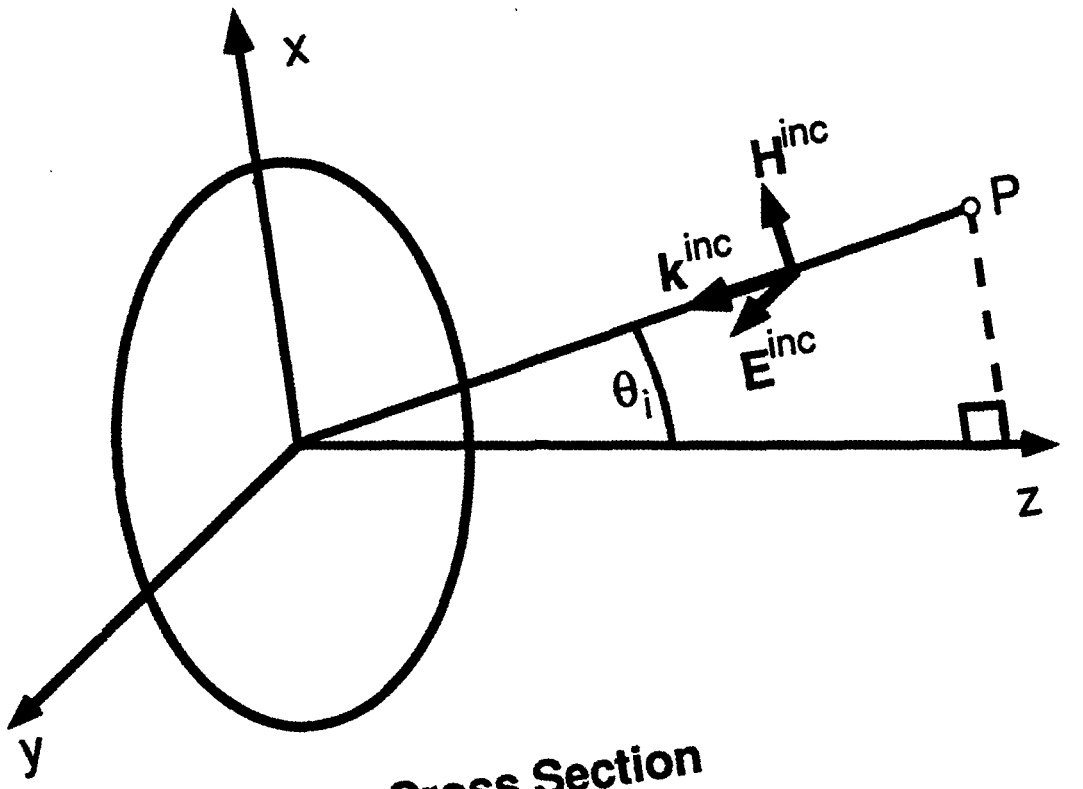

The Backscattering Cross Section

$$\sigma_{BS} = 4\pi R_0^2 \frac{I_{BS}}{I_0}$$

Using a Vector Potential analysis we can write

$$\nabla \times A = \mu_0 H$$

At the point P the Vector Potential is

$$A = \frac{\mu_0}{4\pi} \int_S \frac{[K]}{R} ds'$$

K is the surface current density

$$K = n \times H = 2n \times H^{inc}$$

The Scattered Electric Field Component

$$E_y = -\frac{iE_0}{\lambda R_0}\exp(-ikR_0)\int dx'dy'\left(\cos\theta_i - \frac{\partial h'}{\partial x'}\sin\theta_i\right)\exp(i2kh'\cos\theta_i)\exp(i2kx'\sin\theta_i)$$

The Backscattered Intensity is found from a single point correlation of the field component:

$$I_{BS} = \left\langle E_y E_y^* \right\rangle = \frac{I_0}{\lambda^2 R_0^2}\iint dx'dy'dx''dy''F\left(h', h'', \frac{\partial h'}{\partial x'}, \frac{\partial h''}{\partial x''}\right)\exp\left[i2k\sin\theta_i(x' - x'')\right]$$

The Slope-Height Term:

$$F\left(h',h'',\frac{\partial h'}{\partial x'},\frac{\partial h''}{\partial x''}\right)=\left\langle\left(\cos\theta_i-\frac{\partial h'}{\partial x'}\sin\theta_i\right)\left(\cos\theta_i-\frac{\partial h''}{\partial x''}\sin\theta_i\right)\exp[i2k(h'-h'')\cos\theta_i]\right\rangle$$

$$=\cos^2\theta_i\left\langle\exp[i2k(h'-h'')\cos\theta_i]\right\rangle$$

$$-\sin\theta_i\cos\theta_i\left\{\left\langle\frac{\partial h'}{\partial x'}\exp[i2k(h'-h'')\cos\theta_i]\right\rangle+\left\langle\frac{\partial h''}{\partial x''}\exp[i2k(h'-h'')\cos\theta_i]\right\rangle\right\}$$

$$+\sin^2\theta_i\left\langle\frac{\partial h'}{\partial x'}\frac{\partial h''}{\partial x''}\exp[i2k(h'-h'')\cos\theta_i]\right\rangle$$

The Surface Correlation Function

$$r(\rho) = \frac{\langle h' h'' \rangle}{\sigma^2}$$

Gaussian: $r(\rho) = \exp\left(-\rho^2 / l_c^2\right)$

Exponential: $r(\rho) = \exp\left(-|\rho| / l_c\right)$

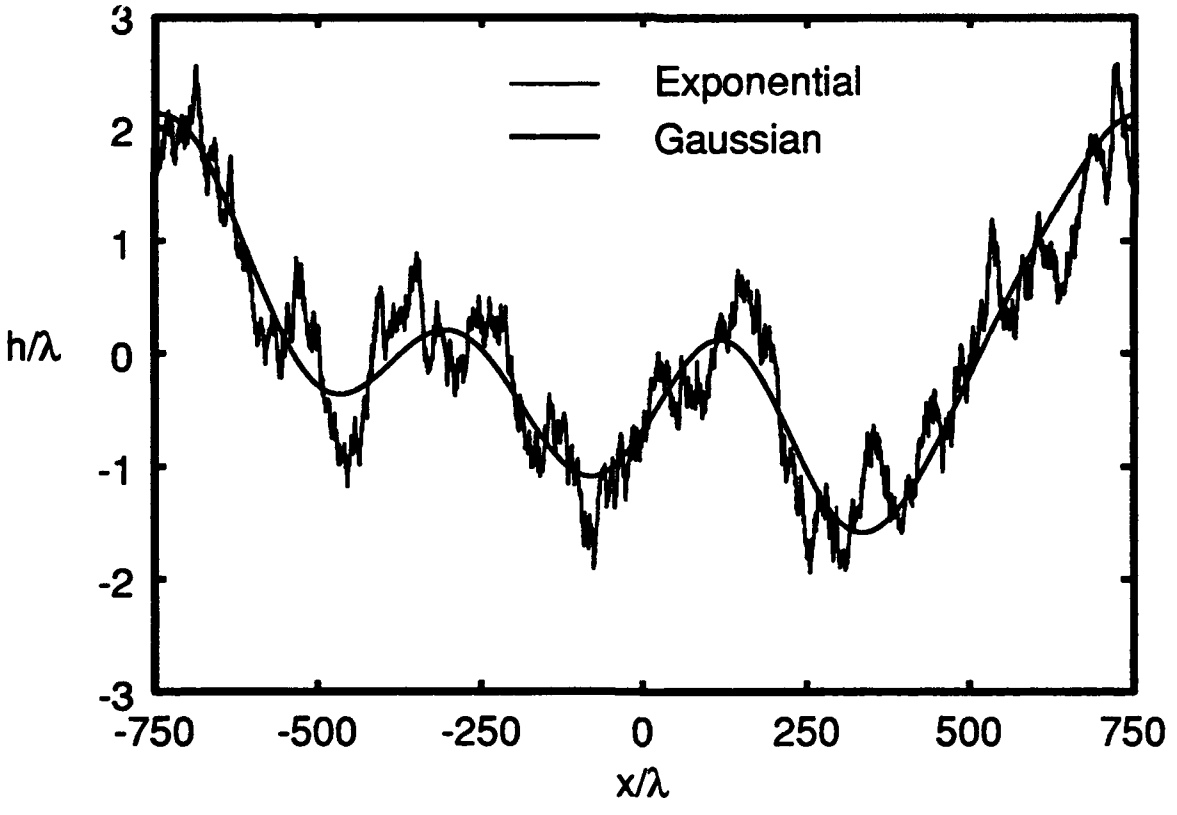

Result for σ_{BS} at $\theta_i=0$

Gaussian surface:

$$\frac{\sigma_{BS}}{\pi a^2} = \left(\frac{l_c}{2\sigma}\right)^2$$

Exponential surface:

$$\frac{\sigma_{BS}}{\pi a^2} = 2\left(\frac{2\pi l_c}{\lambda}\right)^2\left(\frac{\lambda}{2\pi\sigma}\right)^4$$

$$= 2\frac{l_c^2}{k^2\sigma^4}$$

The cross section of the Gaussian surface at normal incidence is much larger than that of the exponential surface.

The cross section of the exponential surface falls off much more rapidly with increasing roughness, σ.

For non-normal incidence we must consider the effects of shadowing.

Shadowing of a surface is a function of the product $\tan\theta_i$ times the rms slope of the surface†

The rms slope is given by $\sigma\sqrt{-\left.\frac{d^2r}{d\rho^2}\right|_{\rho=0}}$

For the Gaussian: $= \sqrt{2}\,\sigma/l_c$

For the exponential surface this formula gives

$$\sigma^2\left(-\frac{d^2r}{d\rho^2}\right) = \frac{2\sigma^2}{l_c}\delta(\rho) - \frac{\sigma^2}{l_c}\exp\left(-|\rho|/l_c\right)$$

The rms slope can be determined from computer simulation and approximation of the delta function. We have found:

The rms slope for the Exponential: $\cong 2.8\,\sigma/\sqrt{\lambda l_c}$

†P. Beckmann, IEEE Trans. Antennas & Propag. **AP-13** (1965).
B. G. Smith, IEEE Trans. Antennas & Propag. **AP-15** (1967).

The Shadowing function is the fraction of the surface that is illuminated at a given incident angle.

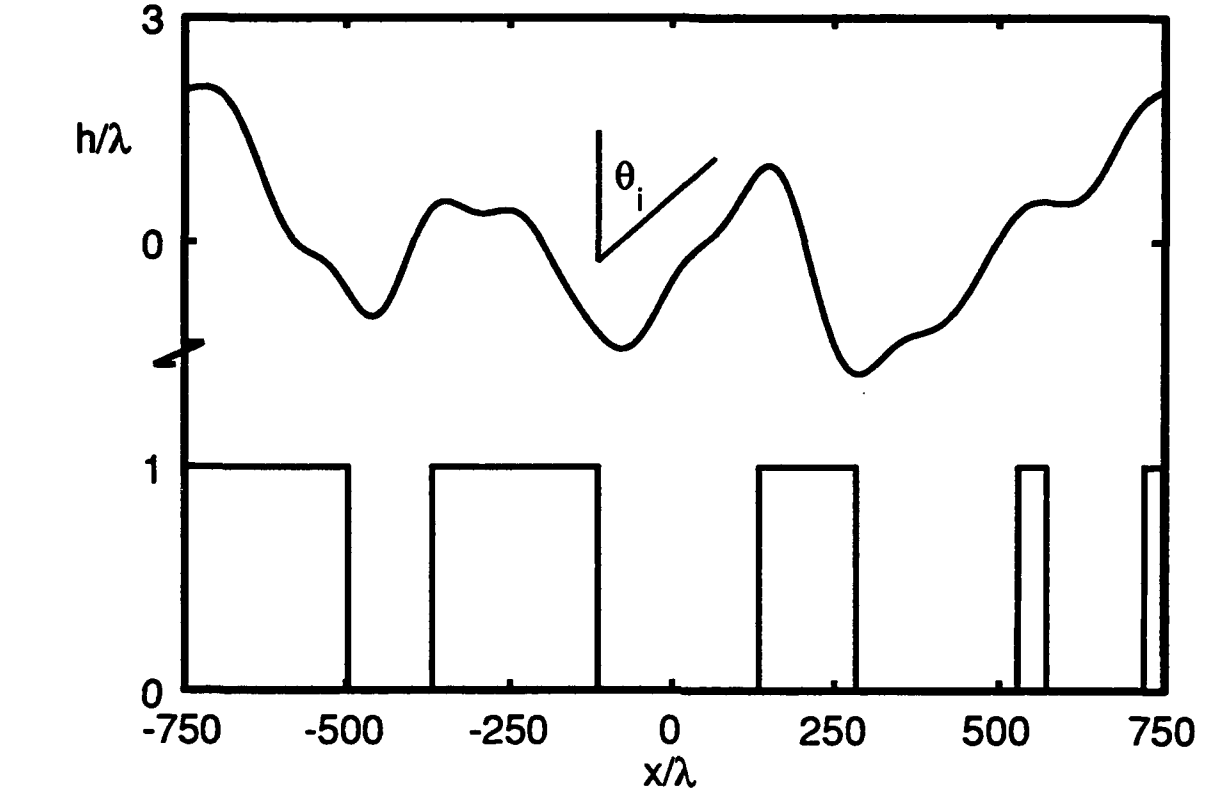

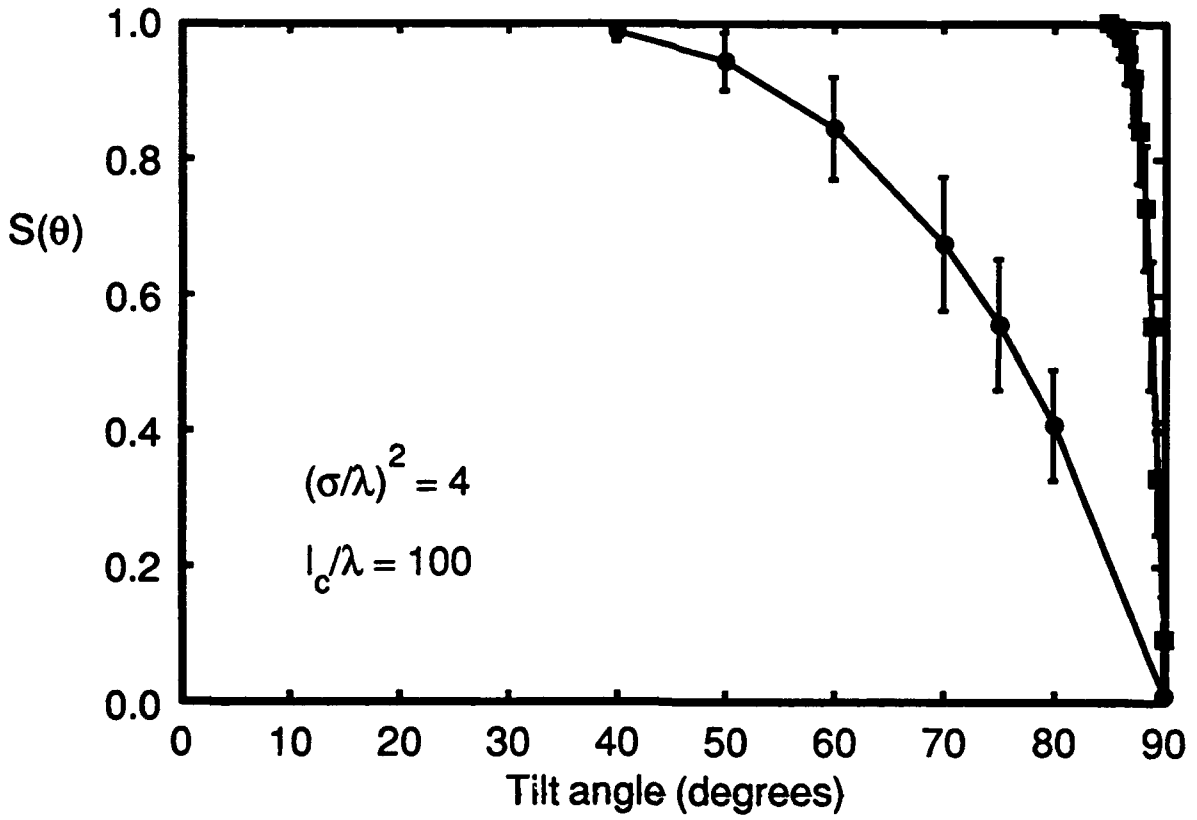

Backscattering Cross Section versus Tilt Angle

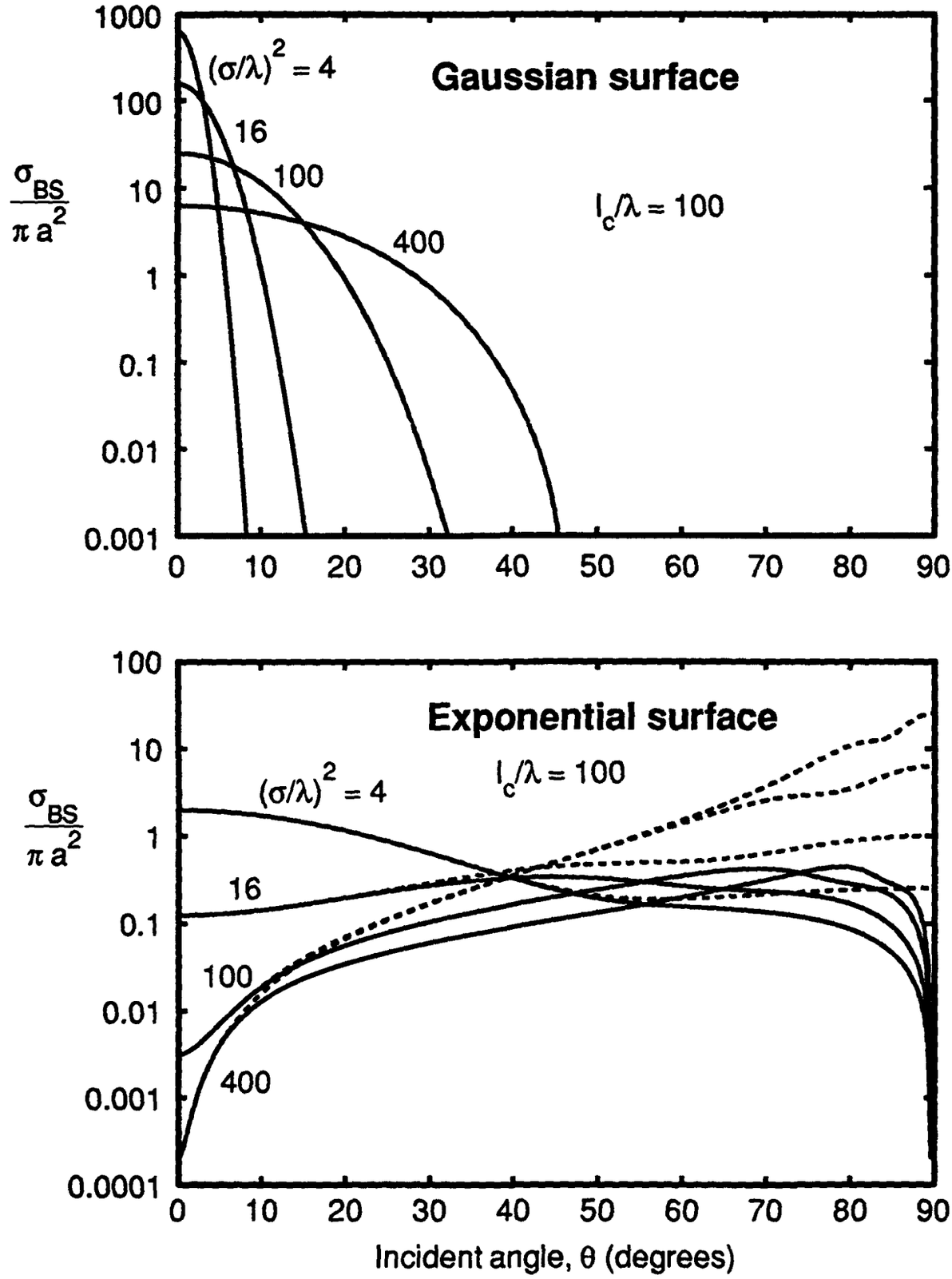

Measured Backscattering Cross Section vs Tilt Angle

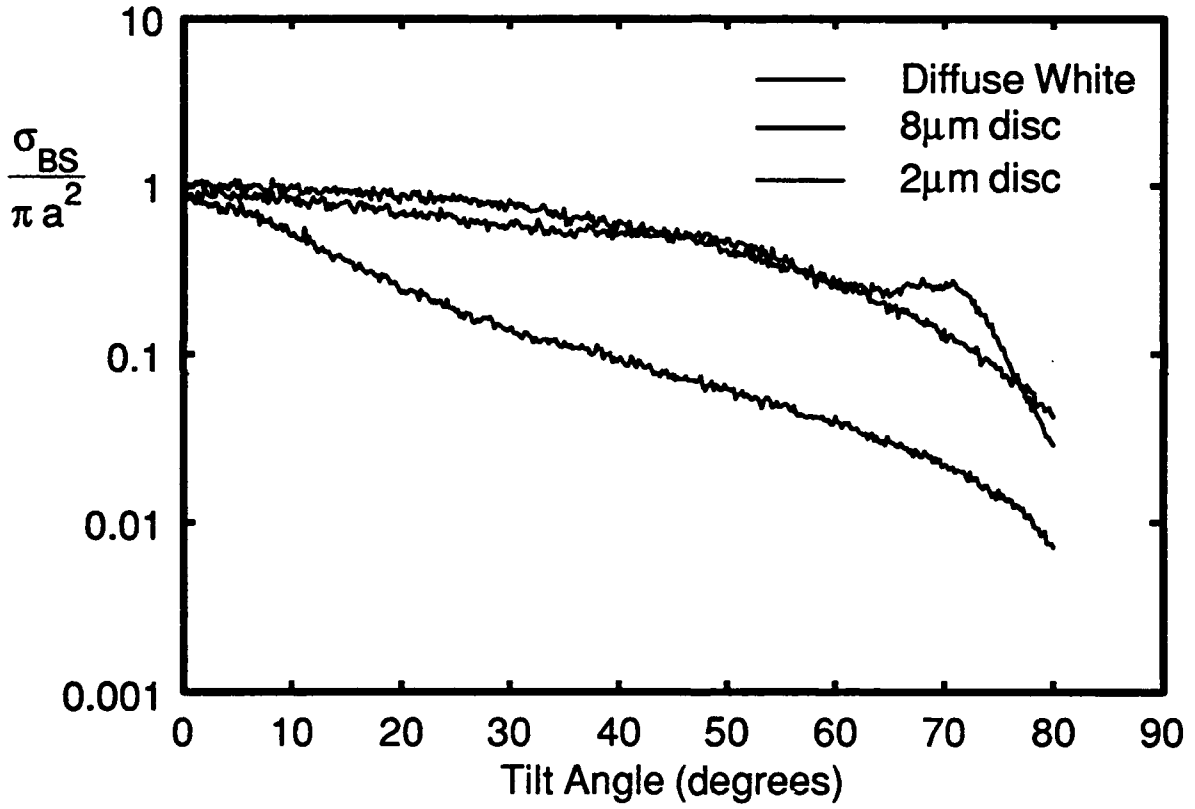

Page 2. Rotating Discs

This series of pictures illustrates the problem. Shown are three discs tilted at various angles to the illumination. The discs are viewed through a beam splitter so that we see the direct backscatter. The tilt angles are a) zero degrees, b) 20°, c) 40° and d) 70°. The large disc has a diffuse white surface. The smaller two are one inch diameter silver discs that have been roughened: the upper left at 2μm rms roughness using a bead-blasting process, and the lower at 8μm using ion-beam etching of a speckle pattern exposed in photo-resist. As the discs are tilted the 2μm disc scatters less and less toward the illuminating direction while the 8μm and diffuse white discs continue scattering strongly. At 70° the 8μm disc is now considerably brighter than the other two. This is explained in terms of the roughness parameters of the discs.

Page 3. Vector Potential

In our analysis the disc is centered at the origin of our coordinate system in the xy plane. It is illuminated with a y-polarized plane wave whose **k** vector lies in the xz plane and forms an angle θ_i with the z-axis. The backscattering cross section is defined as shown where I_{BS} is the backscattered intensity at P a distance R_0 away.

We use a vector potential analysis so that we can write **H** as the curl of the vector potential. At P the vector potential is an integral of the surface current density, **K**. We use these to derive an expression for the far zone electric field.

Page 4. Far Zone Electric Field Component

The far zone y-component of the scattered electric field is given. The integral is over the *illuminated surface* of the disc and contains terms involving the slope and height of the surface at the point of integration.

The intensity is found by taking an ensemble average of the magnitude squared of the field. We have grouped the terms involving the surface height and slope into the function, F.

Page 5. The Slope-Height Term

The function F is the ensemble average of the slope and height terms at two surface points. It can be expanded to three terms as shown. The $\cos^2$ factor is the result for a smooth surface, i.e., h=0. The average of the exponential term is the joint characteristic function of the two heights, h' and h". The other terms affect the result for non-normal incidence due to the sine term. The first of these two terms contains averages of the slope at a given point times the phase difference between two surface points. The last term correlates the slope at two points with this phase difference.

To fully evaluate this expression we require a surface correlation function.

Page 6. Surface Correlation

The surface correlation function is given by the normalized ensemble average of the heights where σ is the rms height variation and ρ is the distance between h' and h". We have assumed that h is characterized by a stationary Gaussian random process. The correlation length is denoted by l_c. We have examined two types of surface correlations: a Gaussian and an exponential. The graph illustrates the difference between these surfaces. The Gaussian has slowly varying and continuous slopes while the exponential has steep and discontinuous slopes.

Page 7. On-axis Results

The on-axis results for the backscattering cross section for the two surfaces are given. These hold for $\sigma \gg \lambda$. We note that the result for the Gaussian surface is independent of wavelength while the exponential result varies as λ^2. Also, the Gaussian result is much larger than that of the exponential. The cross section for the exponential surface falls off rapidly with increasing roughness, σ.

To determine the off-axis cross section we must consider the effect of shadowing.

Page 8. Shadowing

The shadowing of a surface is a function of the product $\tan\theta_i$ with the rms slope of the surface. The rms slope is proportional to the square root of the second derivative of the correlation function. For the Gaussian surface this evaluates to the result shown. For the exponential surface, however, the second derivative of the correlation function gives a delta function at the origin. The rms slope can be evaluated by simulating exponential surfaces on a computer and approximating the delta function based on minimum resolvable surface features. We have found that the rms slope for the exponential surface is given approximately by the result shown. We see that this value is much larger than that for the Gaussian surface as was demonstrated on page 6.

Page 9. Shadowing continued

These results are used to determine a shadowing function which is the fraction of the surface which is illuminated at a given incident angle. Shown in the top graph is a simulated surface illuminated at θ_i. Below this is a function indicating by the value of 1 those portions which are illuminated and by 0 those which are in shadow. Thus ~50% of the surface is illuminated at this angle. Carrying this out for other angles and over many surfaces we obtain an average shadowing function $S(\theta)$ shown in the lower graph for the rms roughness and correlation length given. The exponential surface is represented by circles and the Gaussian by squares. For the same roughness parameters significant shadowing occurs at a much smaller angle for the exponential surface than for the Gaussian. We use this shadowing function in the result for the backscattering cross section for large incident angles.

Page 10. The Backscattering Cross Section

The results for the backscattering cross section versus tilt or incident angle are shown for both types of surfaces. Each is given for a fixed correlation length and for four values of the rms height. The normalized cross section is plotted on a logarithmic scale. The Gaussian cross sections fall off with increasing tilt angle, yet requiring a larger tilt angle for the fall-off to occur with increasing roughness. For the ranges shown no significant shadowing occurs.

For the exponential surface we have included two sets of results: those where we have included shadowing in the calculation, signified by the solid lines and those without shadowing indicated by the dashed lines. The cross section remains significant for all the roughnesses shown at nearly all angles of illumination. For large roughnesses the cross section actually increases with tilt angle.

Page 11. Measured Results

Shown here are the measured backscattering cross sections of the three discs shown on Page 2. The diffuse white surface exhibits the $\cos^2$ behavior of a blackbody scatterer. The 2μm disc shows a more rapid fall off yet still has a substantial value at large angles. The 8μm disc follows the diffuse white disc up to about 60° where it begins to increase up to ~70° and then falls off again. The large cross section at 0° and the increase at large angles indicates that this surface may be a composite surface containing both Gaussian and exponential correlation components.

IMAGE DEBLURRING FOR MULTIPLE-POINT IMPULSE RESPONSES

IMAGE DEBLURRING FOR MULTIPLE-POINT IMPULSE RESPONSES

Bryan J. Stossel and Nicholas George

Institute of Optics
University of Rochester
Rochester, NY 14627

ABSTRACT

We present analysis for the recovery of intensity images degraded by an incoherent point spread function (psf) consisting of a set of randomly distributed impulses. In initial experiments with as many as 100 irregularly spaced impulses we obtain excellent recovery of the original object provided we have precise knowledge of the psf. In practice, there is little or no difficulty presented by the zeros of the multiple point blur transfer function. We describe some interesting methods of counting these zeros over an appropriate region of the transform plane. In the second portion of our presentation particular emphasis is placed on the effects of errors made in the determination of the point spread function. We simulate measurement errors in the recording of the psf by randomly perturbing the location of each impulse about the actual position used to create the blurred image. Analysis and reconstructions based on variations in the measured psf are presented. Examples include the statistical deviation of the measured impulses from their true locations and the number of impulses present in the degradation.

Image Deblurring for Multiple-Point Impulse Responses†

Bryan J. Stossel
Nicholas George

Institute of Optics
University of Rochester

†This Research is Supported by the US Army Research Office

Presented at the 1991 annual meeting of the Optical Society of America
San Jose, Ca.

IMAGING MODEL:

OBJECT SPACE:

$$g(x,y) = f(x,y)*h(x,y) + n(x,y)$$

where

g(x,y) = observed image
f(x,y) = original object scene
h(x,y) = impulse response
n(x,y) = noise

FREQUENCY SPACE:

$$G(f_x,f_y) = F(f_x,f_y)\,H(f_x,f_y) + N(f_x,f_y)$$

MULTIPLE-POINT DEGRADATION:

$$h(x,y) = \sum_{n=0}^{N} \delta(x - x_n)\delta(y - y_n)$$

$$H(f_x,f_y) = \sum_{n=0}^{N} e^{-i2\pi(f_x x_n + f_y y_n)}$$

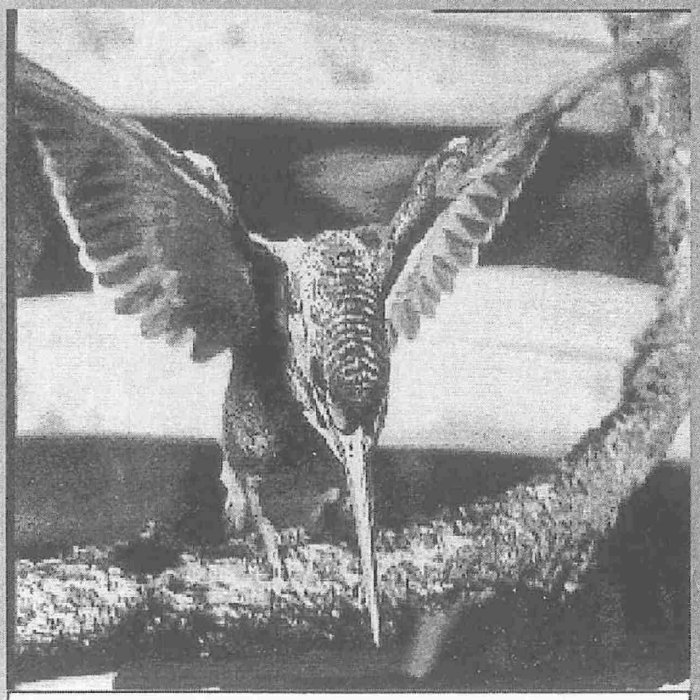

original object

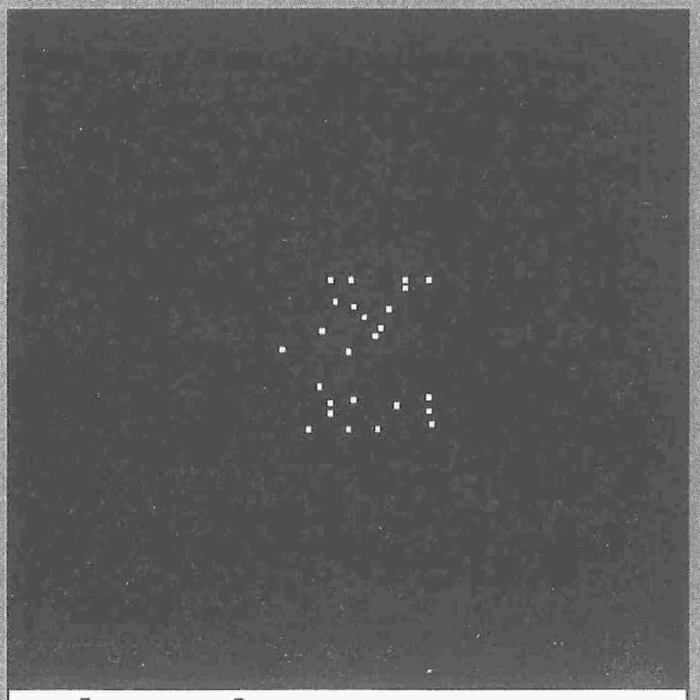

impulse response

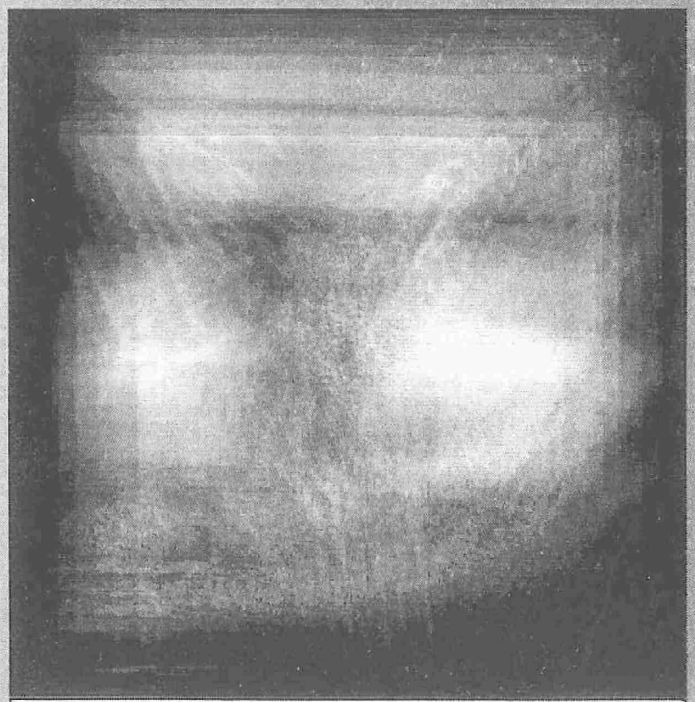

blurred image

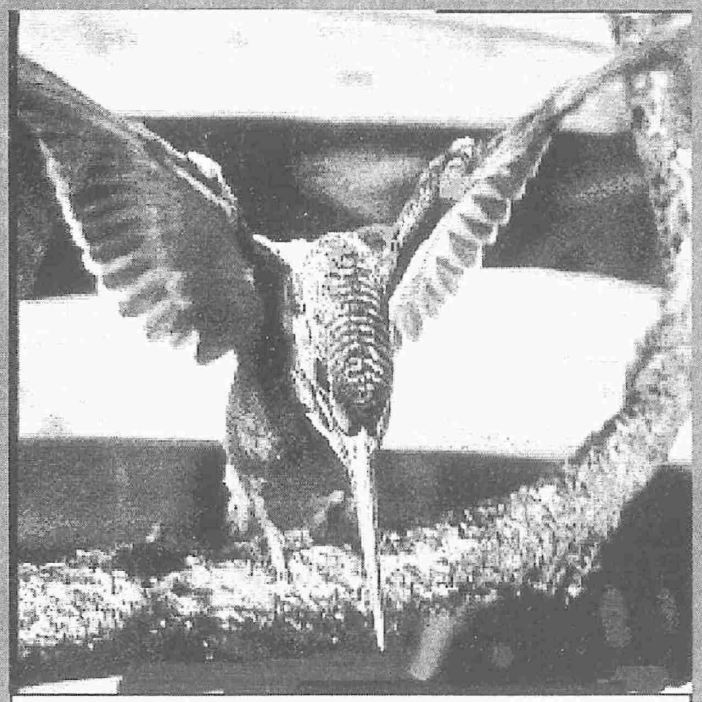

reconstruction

CHARCTERIZATION OF THE DEGRADATION TRANSFER FUNCTION

ZEROS OF THE TRANFER FUNCTION

$$H(f_x, f_y) = \sum_{n=0}^{N} e^{-i2\pi(f_x x_n + f_y y_n)}$$

$$H(f_x, f_y) = R(f_x, f_y) + iX(f_x, f_y)$$

$$R(f_x, f_y) = \sum_{n=0}^{N} \cos\left[2\pi(f_x x_n + f_y y_n)\right]$$

$$X(f_x, f_y) = \sum_{n=0}^{N} \sin\left[2\pi(f_x x_n + f_y y_n)\right]$$

$$H(f_x, f_y) = 0 \quad \Rightarrow \quad R(f_x, f_y) = X(f_x, f_y) = 0$$

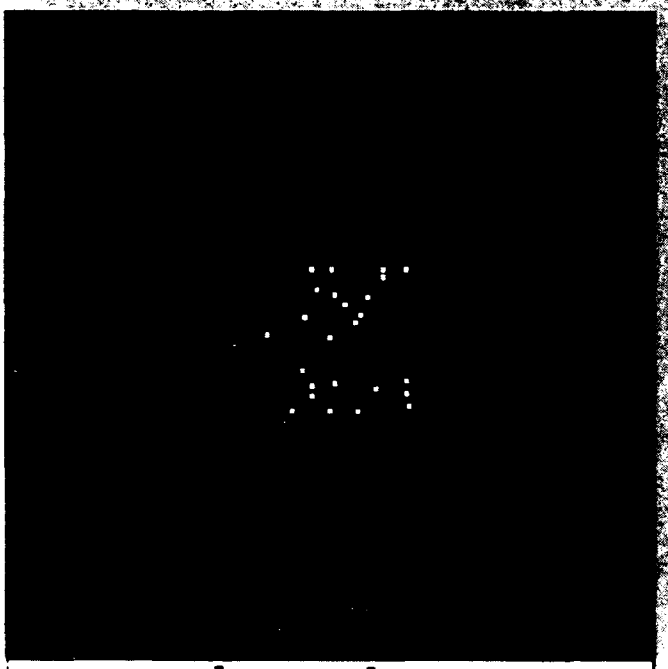

impulse response

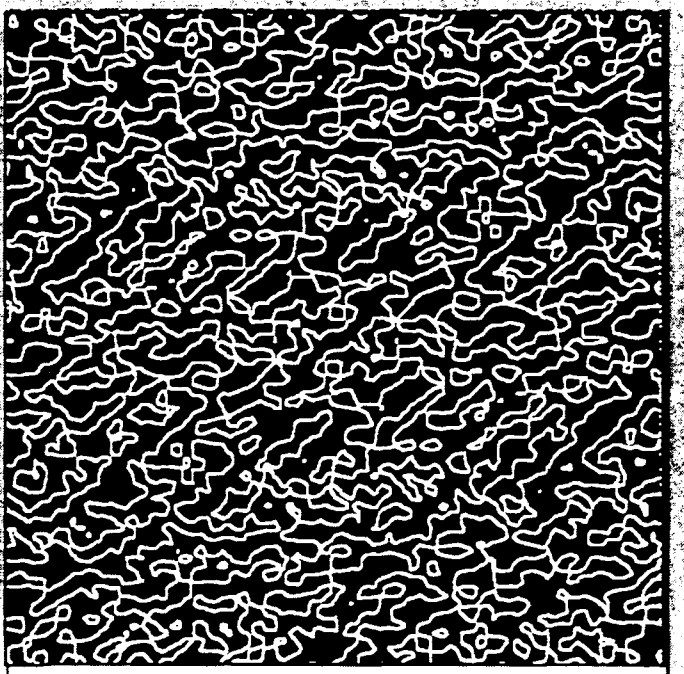

OTF zero contours - real part -

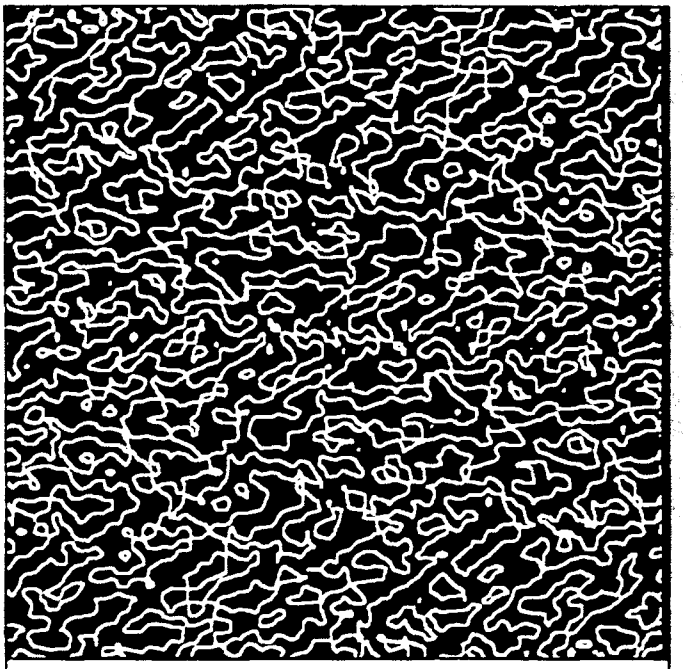

OTF zero contours - imaginary part -

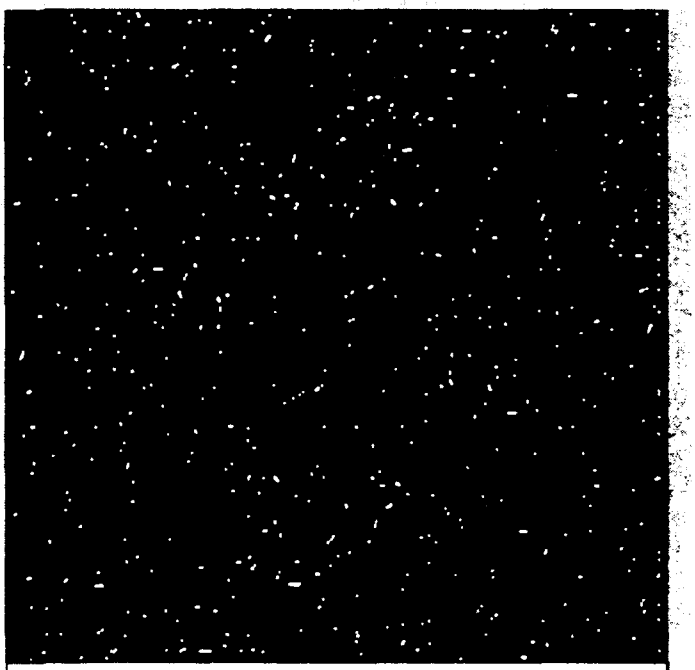

OTF zero contours - magnitude -

RECOVERY EFFECTS OF PSF ERRORS

INCORRECTLY POSITIONED IMPULSES

degradation psf:

$$h(x,y) = \sum_{n=0}^{N} \delta(x - x_n)\delta(y - y_n)$$

recovery psf:

$$\hat{h}(x,y) = \sum_{n=0}^{N} \delta(x - x_n - \Delta_n)\delta(y - y_n - \beta_n)$$

$$\frac{H(f_x, f_y)}{\hat{H}(f_x, f_y)} = \frac{\sum_{n=0}^{N} e^{-i2\pi(f_x x_n + f_y y_n)}}{\sum_{n=0}^{N} e^{-i2\pi[f_x(x_n+\Delta_n)+f_y(y_n+\beta_n)]}}$$

Δ_n, β_n chosen such that:

$$\overline{\Delta}_n = \overline{\beta}_n = 0 \qquad \sigma^2_{\Delta_n} = \sigma^2_{\beta_n} = 4 \text{ pixels}$$

INCORRECT KNOWLEGDE OF THE PSF

POSITIONING ERRORS - 25 PT PSF

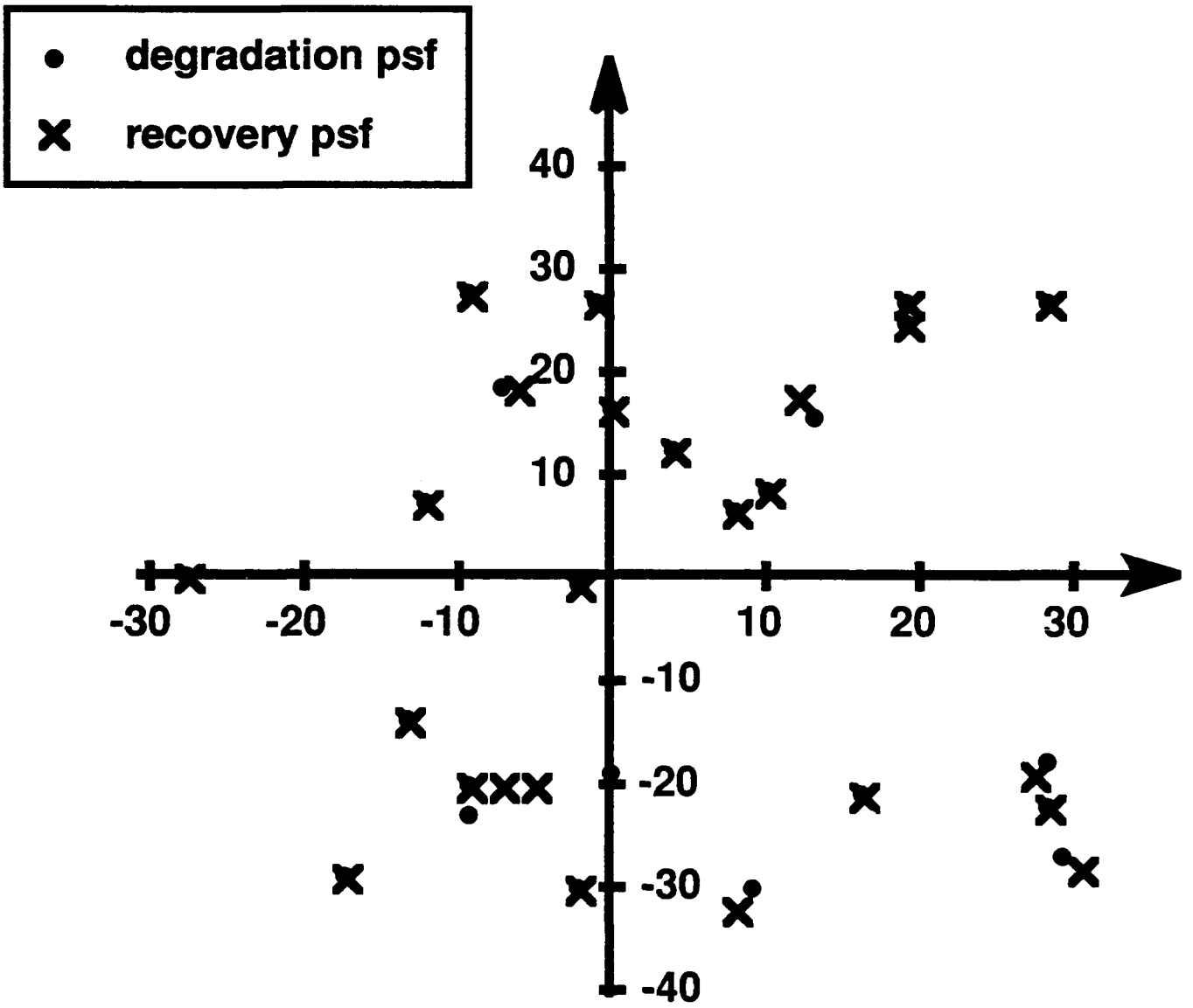

10 pts w/ incorrect positions

$$\sigma_x^2 = \sigma_y^2 = 4 \text{ pixels}$$

RECOVERY EFFECTS OF PSF ERRORS

MAGNITUDE ERRORS

$$h(x,y) = \sum_{n=0}^{N} \delta(x - x_n)\delta(y - y_n) \qquad H(f_x, f_y) = \sum_{n=0}^{N} e^{-i2\pi(f_x x_n + f_y y_n)}$$

$$\hat{h}(x,y) = \sum_{n=0}^{N} a_n \delta(x - x_n)\delta(y - y_n) \qquad \hat{H}(f_x, f_y) = \sum_{n=0}^{N} a_n e^{-i2\pi(f_x x_n + f_y y_n)}$$

$$\frac{H(f_x, f_y)}{\hat{H}(f_x, f_y)} = \frac{\sum_{n=0}^{N} e^{-i2\pi(f_x x_n + f_y y_n)}}{\sum_{n=0}^{N} a_n e^{-i2\pi(f_x x_n + f_y y_n)}}$$

a_n chosen such that:

$$\bar{a}_n = 160 \qquad \sigma^2_{a_n} = 140$$

$$\min\{a_n\} = 10$$

$$\max\{a_n\} = 252$$

Effects of Impulse Response Errors

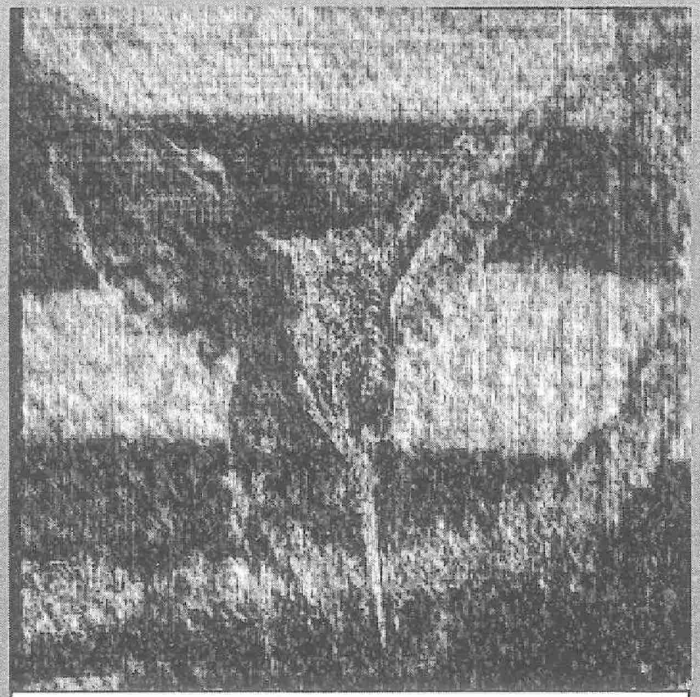

25 pt psf
10 position errors
$\sigma_r^2 = 4$ pixels

25 pt psf
25 magnitude errors
mean = 160 : $\sigma_m^2 = 140$

Summary Remarks

1) The zeros of the transfer function occur at isolated points -- their effects on reconstruction are greatly reduced.

2) Knowledge of the locations of the impulses is critical to the reconstruction.

3) Knowledge of the magnitudes of the impulses is not critical to the recovery.

Page 1:

Our research is concerned with investigating the recovery of intensity images that have been degraded by a point spread function (psf) consisting of a set of irregularly spaced impulses. Our interest in this problem two-fold:

A) There are some interesting aspects involved with characterizing the transfer function. In particular we are concerned about the number and distribution of the zeros in the transfer function.

B) We feel that this problem may have application to the problem of imaging through turbulence.

Page 2:

We are assuming a linear intensity based imaging system where the observed intensity image, $g(x,y)$, is modeled as the convolution of the original scene intensity image, $f(x,y)$, with an intensity psf, $h(x,y)$, plus an additive noise term, $n(x,y)$. For our problem, we are considering a particular psf consisting of irregularly spaced impulses placed at (x_n,y_n).

Page 3:

To illustrate this problem we have chosen a picture of a humming bird because of the details present in the wing and neck feathers as well as the low frequency regions in the background. A typical psf is shown here with 25 pts placed within a 64 x 64 pixel region where the image size is 256 x 256 pixels. The resulting blurred image is shown in the lower left while the recovered image is in the lower right.

Page 4:

Our primary interest in this is to characterize the transfer function. One particular area of interest is to study the number and distribution of zeros in the transfer function. If the transfer function, $H(f_x,f_y)$ is rewritten in terms of the real part, $R(f_x,f_y)$, and the imaginary part, $X(f_x,f_y)$, where R and X are real functions, then in order for $H(f_x,f_y)$ to be zero both $R(f_x,f_y)$ and $X(f_x,f_y)$ must be simultaneously zero.

Page 5:

The real part and the imaginary part are three-dimensional functions and therefore we expect the zeros to form a set of closed-contours. These contours are shown here. The zeros of the transfer function are given by the intersection of these two sets of curves and thus, in general are expected to be isolated points.

Page 6:

We are also interested in the effects of various errors in our knowledge of the degadation psf. One such error is due to incorrect positioning of the impulses. Errors (Δ_n,β_n) were applied to the impulses

where $\bar{\Delta}_n = \bar{\beta}_n = 0$ and $\sigma^2_{\Delta_n} = \sigma^2_{\beta_n} = 4\,\text{pixel}$.

Page 7:

The effects of these position errors can be seen when the degradation psf is plotted along with the psf used in the recovery.

Page 8:

Another source of error can arise in measuring the magnitude of the impulses. To simulate such errors, the magnitudes of the recovery impulses $\{a_n\}$ were set such that $\bar{a}_n = 125$ and $\sigma_{a_n} = 75$, resulting in magnitudes in the range 10 to 252.

Page 9:

The effects of these two sources of error can be seen in the recovered images. Clearly, having correct knowledge of the positions of the impulses is more critical than knowledge of the amplitudes.

Page 10 (Summary)

1) The zeros in the transfer function of the multiple point psf occur in general at isolated points and therefore present little difficulty in the reconstruction problem.

2) Knowledge of the correct positions of the impulses is more critical than knowledge of their magnitudes.